Received: Added at production | Revised: Added at production | Accepted: Added at production

DOI: xxx/xxxx

RESEARCH ARTICLE

An idealised model of convective hydration of the Tropical Tropopause Layer. Part II: the role of convective intensity, turbulent mixing, sedimentation and vertical shear

Charles W. Powell | **Peter H. Haynes** | **John R. Taylor**

[1]Department of Applied Mathematics and Theoretical Physics, University of Cambridge, Centre for Mathematical Sciences, Wilberforce Road, Cambridge, CB3 0WA

Correspondence
Corresponding author: Charles Powell.
Email: cwp29@cam.ac.uk

Abstract

Deep convective plumes overshooting into the Tropical Tropopause Layer (TTL) bypass the cold-point temperature constraint on water vapour concentrations, providing an important but poorly constrained pathway for hydrating the tropical lower stratosphere. We investigate the mechanisms controlling convective hydration of the TTL using large-eddy simulations of a scaled-down flow in which a turbulent buoyant plume carrying temperature-dependent tracers penetrates into a stably stratified layer. Part I validated the moisture scheme and numerical model, demonstrating the key role of turbulent mixing between cold, ice-rich fluid in the plume and the warmer surroundings, resulting in sublimation of ice to produce an excess hydration unless limited by downward sedimentation of ice. Here, we show how convective intensity and large-scale vertical shear modulate this balance. Consistent with other modelling studies, we find that stronger convective intensity significantly enhances total hydration. More intense plumes penetrate deeper into the stably stratified layer, accessing warmer environmental air, while simultaneously sustaining stronger central updrafts that delay ice sedimentation, allowing increased sublimation of ice. Additionally, the presence of large-scale vertical shear increases the total hydration. Environmental shear stretches the intense mixing region at the top edge of the penetrating plume cap into the downstream intrusion, thereby exposing more plume fluid to warmer environmental air. Whilst turbulent mixing is primarily driven by the large buoyancy difference between the penetrating plume and its surroundings, gravity wave breaking and shear instabilities can increase hydration by further promoting mixing. Our results demonstrate that convective hydration is sensitive to the size of ice crystals via their sedimentation velocity, as well as the dynamic influence of the convective source strength and environmental wind shear.

KEYWORDS
Tropics, Stratosphere, Convection, Moisture, Numerical simulations, Turbulent mixing

1 | INTRODUCTION

In the tropics, particularly strong deep convection that overshoots into the tropical tropopause layer (TTL) can irreversibly transport moisture by avoiding the cold-point constraint on water vapour concentrations (Randel and Jensen, 2013). Moist anomalies slowly rise into the tropical lower stratosphere (TLS) above, providing a secondary but non-negligible route for hydration of the TLS alongside slow quasi-horizontal upwelling (Powell et al., 2025a). As a gateway to the wider stratosphere via the Brewer-Dobson circulation, convective hydration of the TTL has consequences for global stratospheric composition (Butchart, 2014; Fueglistaler et al., 2009).

Convective hydration of the TTL occurs as a result of turbulent mixing between cold, ice-rich air in the overshoot and warmer, subsaturated air in the TTL that warms mixed fluid parcels and results in the sublimation of ice, producing anomalous vapour concentrations. There are several factors that directly control the extent to which hydration occurs. For example, it has been shown that the TTL environment must be subsaturated for a net hydration to occur (Hassim and Lane, 2010). The

influence of other factors, particularly those that interact with or modify turbulent mixing, such as downward sedimentation of ice, the strength of convective forcing, and large-scale vertical shear surrounding the overshoot, is less clear. The strength of convective forcing influences the transport of vapour and ice into the stratified layer as well as the penetration height of the plume. Sedimentation modulates this transport by determining whether ice remains in suspension in the plume and therefore whether ice is available to sublimate following mixing between the plume and environment. Large-scale vertical shear has been proposed to influence hydration by modulating the vortical response to convective penetration (Lane, 2008) as well as turbulent mixing, via (internal) gravity wave breaking (Hassim and Lane, 2010; Lane et al., 2003; Lane and Sharman, 2006; Sang et al., 2018) and shear instabilities at the cloud edge (Dauhut et al., 2018). Previous studies have sought to address the influence of these processes using numerical simulations of individual convective overshoots (or collections thereof) using comprehensive meteorological models with observed environmental setups (Hassim and Lane, 2010; Sang et al., 2018; Dauhut et al., 2018; O'Neill et al., 2021). Whilst realistic and directly comparable with observations, these studies are limited to a small set of computationally expensive simulations in which small-scale turbulent mixing is parameterised. Thus only a narrow set of regimes can be explored, which is not necessarily representative of the breadth of regimes present in the TTL, and for which interpretation of the interaction between processes is difficult.

In Part I, we introduced an idealised model of this problem, in which a turbulent buoyant plume rises through a uniform layer and penetrates into a linearly stably stratified layer carrying passive tracers that represent vapour and ice which are exchanged via condensation/sublimation, and ice sediments downward at a fixed velocity. We use large-eddy simulations of a scaled-down model flow, such that a more significant portion of the turbulent spectrum is resolved and a wider range of simulations can be considered with limited computational resources. Moreover, by including only essential processes that have been identified to play a role in controlling vapour transport, the interaction between processes is more straightforward to interpret. In this paper, we consider a set of three experiments to investigate the role of convective intensity, sedimentation, and large-scale vertical shear in controlling convective hydration of the TTL. The simulations presented in this paper are organised into one control run and three experiments, each with a single parameter varied relative to the control simulation that determines (1) the sedimentation strength, (2) the plume forcing strength, and (3) the vertical shear rate of the mean flow in the stratified layer. Within each experiment, parameter values are chosen such that the process under consideration is weak, influential, and dominant relative to characteristic properties of the plume. We use the regime numbers $R_{\mathrm{H}}, R_{\mathrm{S}}$, and R_{SH} introduced in Part I to quantify the regime in each simulation. To place our results in the context of the literature on convective hydration of the TTL, we primarily refer to three studies: Hassim and Lane (2010), henceforth referred to as H10; Dauhut et al. (2018), henceforth D18; and Sang et al. (2018), henceforth S18. As in our simulations, these studies consider large-eddy simulations that parameterise the effects of sub-grid-scale (SGS) turbulence, but as discussed in Part I our results are less sensitive to the SGS turbulence model and the representation of turbulent mixing is more realistic.

The paper is laid out as follows. In § 2 we detail the experimental design, including the choice of simulation parameters based on corresponding quantities in the TTL. We explore the control simulation in § 3 and introduce metrics used to assess tracer transport and turbulent mixing. Experiment 1 with varied sedimentation velocity in § 4 is similar to that presented in Part I, where it was shown that sedimentation and mixing compete to determine hydration. Here, we show that the distribution of vapour concentrations can be modelled using parcel trajectories given knowledge of the relative sizes of the sedimentation velocity and the typical turbulent eddy vertical velocity. In experiment 2 in § 5, a subset of the simulations in experiment 1 are repeated with stronger plume forcing. We verify the hypothesis by D18 that convective intensity directly influences hydration by controlling the maximum penetration height of the overshoot, which determines the warmest environmental fluid accessible to the plume via mixing. Large-scale vertical shear is introduced in experiment 3 in § 6. We examine its influence on hydration and turbulent mixing using the buoyancy-tracer volume distribution formalism detailed in Part I (Powell et al., 2024). We show that strong environmental shear enhances turbulent mixing by promoting shear instabilities and internal gravity wave breaking. In § 7 we summarise our findings.

2 | EXPERIMENTAL DESIGN

The simulation setup and numerical method are as described in Part I. Simulation parameters for each experiment and the names used to refer to individual simulations are shown in table 1. As in Part I, values in the figures and text are given in the geophysical scale relevant to the TTL, as opposed to simulation values, unless otherwise stated. We restrict attention to the model regime $R_{\mathrm{H}} \gg 1$ since it is representative of the atmospheric case, where convective overshoots penetrate into the TTL carrying significant concentrations of ice (i.e. 'ice-rich' or 'ice-loaded'), as discussed in Part I. We use a reference saturation concentration

Simulation	N_h	L_h (m)	t_{end} (s)	F_0 ($\times 10^{-6}$) (m^4s^{-3})	w_s (m s^{-1})	R_{S}	λ (s^{-1})	R_{SH}
`control`	512	0.6	35	5	0	0	0	0
`weak_sed`	512	0.6	35	5	5×10^{-4}	0.06	0	0
`sed`	512	0.6	35	5	5×10^{-3}	0.6	0	0
`strong_sed`	512	0.6	35	5	5×10^{-2}	7.2	0	0
`control+F`	512	0.6	35	20	0	0	0	0
`sed+F`	512	0.6	35	20	5×10^{-3}	0.45	0	0
`strong_sed+F`	512	0.6	35	20	5×10^{-2}	4.0	0	0
`weak_shear`	1024	0.8	15	5	0	0	0.175	0.30
`shear`	1024	0.8	15	5	0	0	0.5	0.93
`strong_shear`	1024	0.8	15	5	0	0	1.2	2.0

TABLE 1 Simulation parameters. Values given for the simulated scale. The parameters $N_0 = 1\,\text{s}^{-1}$, $F_0^{(\phi)} = 5 \times 10^{-6}\,\text{m}^3\text{s}^{-1}$, $\phi_0 = 0.2$, $t_{\text{lim}} = 10\,\text{s}$, $N_z = 513$ and $L_z = 0.5\,\text{m}$ are fixed. The mean attained plume buoyancy and tracer fluxes are $F_0^{(\phi)} = 5.5\times10^{-8}\,\text{m}^3\text{s}^{-1}$ and $F_0 = 5.5\times10^{-8}\,\text{m}^4\text{s}^{-3}$ in the control forcing simulations and $F_0 = 3.0\times10^{-7}\,\text{m}^4\text{s}^{-3}$ and $F_0^{(\phi)} = 7.5\times10^{-8}\,\text{m}^3\text{s}^{-1}$ in the strong forcing simulations.

$\phi_0 = 0.2$, yielding an average $R_{\text{H}} \approx 12$ in simulations with the control plume forcing value shown in table 1. Simulations with the strong plume forcing value yield an average $R_{\text{H}} \approx 5$: the plume is more buoyant, hence warmer, so can support larger vapour concentrations, reducing R_{H}. The environmental setup (i.e. H, N_0^2, and the initial condition $\phi_v = \phi_c = \phi_p = 0$) is fixed between simulations. The plume is forced up to time $t \leq t_{\text{lim}} = 400\,\text{s}$ as in Part I but the simulation length is extended to time $t = t_{\text{end}} = 1400\,\text{s}$. The longer simulation time introduces an additional 'relaxation' stage of the flow evolution that follows after plume forcing ceases and the plume cap collapses. During the relaxation stage, environmental buoyancy contours relax to their initial positions and re-establish the stratification that was disturbed by the penetrating plume. This setup can be considered representative of atmospheric convection initiated by a finite release of buoyant fluid (i.e. a thermal) and has been used in previous numerical studies of convective hydration (Hassim and Lane, 2010; Sang et al., 2018). Running simulations for longer than the plume is forced provides a clear distinction between cases with varying sedimentation velocity; when w_s is small then the effect of sedimentation is only seen on long timescales. Although radial spreading of the intrusion slows after plume forcing ends, the increased simulation length means that the lateral edge of the intrusion approaches the edge of the (horizontally periodic) domain, but with negligible influence on the flow evolution. Simulations with large-scale vertical shear in § 6 use $t_{\text{end}} = 600\,\text{s}$, so that the plume cannot wrap around the horizontally periodic domain and interact with itself during the simulation.

The experiments are set up as follows. Table 2 gives simulation parameters detailed below at the simulated and the geophysical scale. Characteristic dynamical quantities are also given: the typical turbulent vertical velocity in the plume w_{eddy} (defined formally in Part I), azimuthal average buoyancy and vertical velocity at penetration on the plume centreline $\overline{b}(r = 0, z = 0)$ and $\overline{w}(r = 0, z = 0)$ (averaged over $200 \leq t \leq 400\,\text{s}$), maximum penetration height z_{max}, equilibrium height z_{n}, and dynamical timescale τ_d (as defined in Part I).

1. **Varied sedimentation strength.** The sedimentation velocity w_s is varied to give regimes with $R_{\text{S}} \ll 1$, $R_{\text{S}} \sim 1$ and $R_{\text{S}} \gg 1$ in simulation `weak_sed`, `sed`, and `strong_sed` respectively. Recall that $R_{\text{S}} = w_s/w_{\text{eddy}}$ is the ratio of the sedimentation velocity and the typical turbulent vertical velocity in the plume. Simulation `weak_sed` is representative of the atmospheric case: using data from Grabowski (1998) (their figure 2) for precipitating frozen water, equivalent to ice in our model, the velocity is on the order of $1\,\text{ms}^{-1}$ on atmospheric scales which translates to $w_s = 5 \times 10^{-4}\,\text{ms}^{-1}$ at the simulated scale.
2. **Varied forcing strength.** Simulations `control`, `sed`, and `strong_sed` with $R_{\text{S}} = 0$, $R_{\text{S}} \sim 1$, and $R_{\text{S}} \gg 1$, respectively, are repeated with the source integral buoyancy flux F_0 quadrupled relative to the control simulation. Note that whilst the prescribed source tracer flux is fixed, the simulated source tracer flux is slightly larger compared to the control forcing simulations because the central updraft is stronger.
3. **Varied vertical shear strength.** The vertical shear rate $\lambda = \partial_z u$ is varied to give regimes $R_{\text{SH}} \ll 1$, $R_{\text{SH}} \sim 1$ and $R_{\text{SH}} \gg 1$ in simulation `weak_shear`, `shear`, and `strong_shear`, respectively. Recall that $R_{\text{SH}} = \tau_d/\lambda^{-1}$ is the ratio of the dynamical timescale and the shear timescale. To accommodate the lateral deformation of the plume and intrusion, the domain width is increased to $L_h = 0.8\,\text{m}$ and the horizontal resolution is doubled to $N_h = 1024$. Values of the parameter λ are chosen to cover the wide range of vertical shear rates found in the TTL. The shear rate chosen for the $R_{\text{SH}} \ll 1$ case is calculated from the mean shear between 15 and 18 km, 5°N-S from 2010 to 2015 using ERA5 reanalysis data, giving $\lambda_{\text{atmos}} = 4.4 \times 10^{-3}\,\text{s}^{-1}$ which translates to $\lambda = 0.175\,\text{s}^{-1}$ at the simulated scale. The choice of λ for the $R_{\text{SH}} \gg 1$ regime is

Simulation(s)	Quantity	Simulation value	Geophysical equivalent
All	N_0^2 (s^{-2})	1	6.25×10^{-4}
All	t_{lim} (s)	10	400 (6⅔ min.)
No shear	t_{end} (s)	35	1400 (23⅓ min.)
Shear	t_{end} (s)	15	600 (10 min.)
Control forcing	F_0 ($m^4\ s^{-3}$)	5.5×10^{-8}	2.1×10^{7}
Strong forcing		3.0×10^{-7}	1.1×10^{8}
`weak_sed` (+F)	w_s ($m\ s^{-1}$)	5×10^{-4}	0.875
`sed` (+F)		5×10^{-3}	8.75
`strong_sed` (+F)		5×10^{-2}	87.5
`weak_shear`	λ (s^{-1})	0.175	4.4×10^{-3}
`shear`		0.5	1.3×10^{-2}
`strong_shear`		1.2	3.0×10^{-2}
No shear	w_{eddy} ($m\ s^{-1}$)	7.7×10^{-3}	13.5
No shear (+F)		1.1×10^{-2}	19.3
`weak_shear`		7.1×10^{-3}	12.4
`shear`		9.3×10^{-3}	16.3
`strong_shear`		8.3×10^{-3}	14.5
Control forcing	$\overline{w}(r = 0, z = 0)$ ($m\ s^{-1}$)	3.8×10^{-2}	67
Strong forcing		6.3×10^{-2}	110
Control forcing	$\overline{b}(r = 0, z = 0)$ ($m\ s^{-2}$)	6.3×10^{-3}	0.28
Strong forcing		1.6×10^{-2}	0.70
No shear	z_{max}	5.2×10^{-2} m	3.6 km
No shear (+F)		8.2×10^{-2} m	5.7 km
`weak_shear`		5.1×10^{-2} m	3.6 km
`shear`		5.7×10^{-2} m	4.0 km
`strong_shear`		5.3×10^{-2} m	3.7 km
No shear	z_{n}	1.0×10^{-2} m	0.7 km
No shear (+F)		1.9×10^{-2} m	1.3 km
`weak_shear`		8.1×10^{-3} m	0.6 km
`shear`		1.3×10^{-2} m	0.9 km
`strong_shear`		1.8×10^{-2} m	1.3 km
No shear	τ_d (s)	2.10	84
No shear (+F)		1.80	72
`weak_shear`		1.72	69
`shear`		1.85	74
`strong_shear`		1.68	67

TABLE 2 Conversion of parameters from the simulated scale to geophysical scales representative of the TTL. The scale factors are $R_t = 40$ and $R_l = 7 \times 10^4$ are as derived in Part I.

calculated from observations during Indian summer monsoon (Sunilkumar et al., 2015; Liu, 2017), which give shear rates $\lambda_{\text{atmos}} \approx 3 \times 10^{-2}\ s^{-1}$ that translate to $\lambda = 1.2\ s^{-1}$ at the simulated scale.

In a broad class of stratified shear flows, a criterion for linear instability of infinitesimal perturbations is for the local gradient Richardson number,

$$\text{Ri}_g = \frac{\frac{\partial b}{\partial z}}{\left(\frac{\partial u}{\partial z}\right)^2 + \left(\frac{\partial v}{\partial z}\right)^2}, \tag{1}$$

to be less than 1/4 somewhere in the flow (Howard, 1961; Miles, 1961; Howland et al., 2018). In the shear simulations, initially $\text{Ri}_g = N_0^2/\lambda^2$ in the stratified layer. The minimum value is achieved in simulation `strong_shear`, with $\text{Ri}_0 \approx 0.8$, so shear instability cannot spontaneously develop. However, instabilities may arise where the local shear rate or buoyancy gradient is modified by the penetrating plume, locally enhancing turbulent motions. Internal gravity wave breaking may also lead to the generation of turbulence (Lane and Sharman, 2006). To better resolve these processes, in the shear simulations the grid is modified so that the vertical grid spacing is smaller (i.e. better resolved) between $z = 0$ and $z \approx 10$ km.

3 | CONVECTIVE HYDRATION OF A STABLY STRATIFIED LAYER

In this section we examine the `control` simulation as a reference for the experiments presented in the following sections. We discuss the dynamical evolution of the flow and introduce quantities used to assess mixing and tracer transport in the stratified layer.

3.1 | Evolution of moist tracers and temperature

The dynamical evolution of the flow can be separated into three stages: penetration towards the maximum penetration height $z_{\max}$, collapse of the plume cap once plume forcing ends, and relaxation at late times. Figure 1 shows the time evolution of the vapour concentration ϕ_v, ice concentration ϕ_c, and temperature T in simulation `control`. Recall from Part I that 'plume fluid' refers to regions with $\phi_p \geq 10^{-3}$. 'Undiluted' plume fluid has not yet mixed with the environment, whilst 'mixed' (plume) fluid refers to plume fluid that has been mixed with the environment. We use the term 'moist' to refer to regions with large vapour concentrations ϕ_v, relative to 'dry' regions with small values of ϕ_v, regardless of the ice concentration ϕ_c.

During the penetration stage up to $t \approx 200$ s, the strong central updraft lifts undiluted plume fluid to its maximum penetration height $z_{\max} \approx 3.5$ km. As the central plume rises, a pocket of very cold fluid forms in the plume cap (panel c) that is freeze-dried, i.e. relatively dry (panel a) and loaded with ice (panel b), as in TTL overshooting tops (Dauhut et al., 2018). As the relative buoyancy between plume fluid and the surroundings becomes negative, the plume cap collapses and turbulent mixing occurs between cold plume fluid and the surrounding warm environmental fluid, creating a shell of warmer mixed plume fluid that permits larger vapour concentrations (panel d) as the saturation concentration increases. Correspondingly, the ice concentration decreases (panel e) via sublimation; no sedimentation is present in simulation `control` that would otherwise remove ice and limit the hydration. Further hydration occurs as a result of adiabatic warming as mixed plume fluid descends from the plume cap and begins to spread laterally in the intrusion, as well as further mixing with the environment. Although plume forcing ends at time $t_{\text{lim}} = 400$ s, plume fluid continues to rise through the uniform layer and can still be seen rising beyond the cold point ($z = 0$) at $t = 600$ s in panels (g)–(i). Gravity waves are evident from the perturbation of buoyancy contours above the plume, as well as perturbation of the environmental temperature, in panels (i), (l), and (o). At $t = 1000$ s and $t = 1400$ s the plume has reached the relaxation stage; buoyancy contours gradually relax and mixed plume fluid gradually reaches equilibrium with the environment – note that the plume becomes stratified like the surrounding environment at late times (panel o). At this stage, most of the remaining mixed plume fluid is hydrated compared to the cold plume fluid formed during penetration and ice remains in the plume (panel n), indicating that the mixed plume fluid remains at saturation. Some fluid surrounding the plume is slightly subsaturated, carrying some vapour (panel m) but no ice – here, $\phi_p > 0$ since mixing has occurred between the plume and environment, but ϕ_p is below the 'plume' threshold.

3.2 | Quantifying hydration of the stratified layer

To quantify the evolution of moist and passive tracers, we calculate the total amount of each tracer in the stratified layer at time t. The total amount of tracer ϕ_i is

$$\mathcal{T}_i(t) = \int_{\substack{z \geq -L \\ \phi_i \geq \phi_{i,\min}}} \phi_i(\boldsymbol{x}, t)\, \mathrm{d}V = \int W_i(b, \phi; t)\phi\, \mathrm{d}\phi \mathrm{d}b, \tag{2}$$

where we exclude tracer concentrations $\phi_i \leq \phi_{i,\min}$ to handle numerical artefacts (Gibbs ringing in particular; see Part I). In the following analysis, we use 'total hydration' to mean the final amount of tracer in the stratified layer, $\mathcal{T}_v(t_{\text{end}})$. This is analogous to the 'net hydration' often referred to in the atmospheric literature, but we avoid the term 'net' since there is no initial vapour content in the stratified layer. Transport of vapour into the stratified layer can be separated into direct transport, where vapour is carried by the plume, and indirect transport, where ice is carried by the plume and later sublimated into vapour. The total amount of tracer ϕ_i that has been directly transported into the stratified layer by the plume up to time t is

$$\mathcal{I}_i(t) = \int_0^t \int_{\substack{z=-L \\ \phi_i \geq \phi_{i,\min}}} \phi_i(\boldsymbol{x}, t) w(\boldsymbol{x}, t)\, \mathrm{d}S \mathrm{d}t = \int_0^t \int S_i(b, \phi; t)\phi\, \mathrm{d}\phi \mathrm{d}b \mathrm{d}t. \tag{3}$$

The 'retained fraction' of tracer ϕ_i at time t is then $\mathcal{T}_i / \mathcal{I}_i$, i.e. the total amount of tracer present in the stratified layer at time t as a fraction of the amount directly injected by the plume up to that time. The 'excess hydration fraction' quantifies the indirect

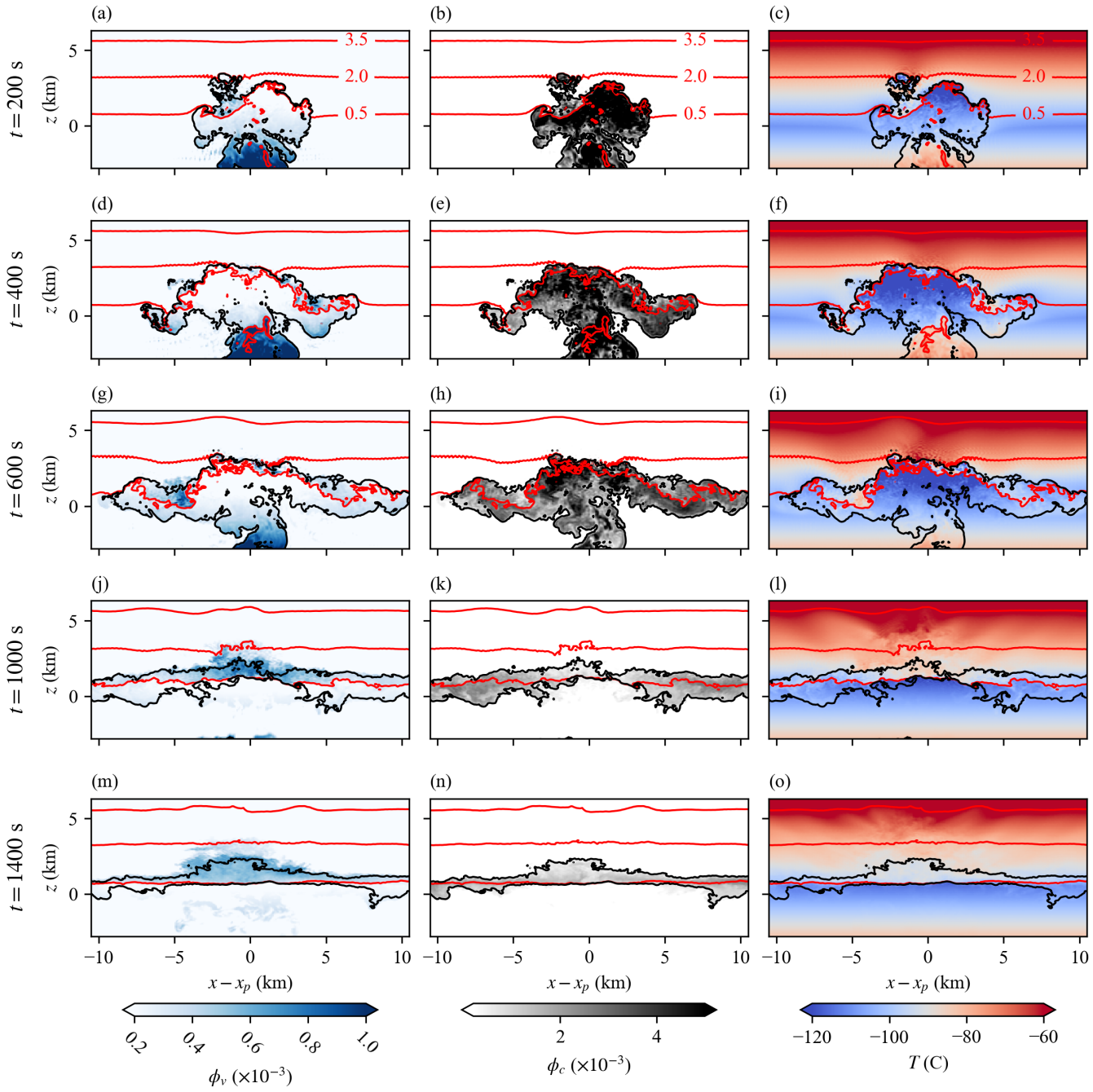

FIGURE 1 Snapshots of simulation `control` showing x-z cross-sections through the plume centreline of the vapour concentration ϕ_v, ice concentration ϕ_c, and temperature T. The black outline indicates the plume contour $\phi_p = 10^{-3}$. In each plot, buoyancy contours are shown in red at 1 m s^{-2} intervals starting from $b = 0.5$ m s^{-2}.

transport as a fraction of the direct transport, defined as the final retained fraction of vapour $\mathcal{T}_v(t_{\text{end}})/\mathcal{I}_v(t_{\text{end}})$. When the excess hydration fraction exceeds unity then the indirect transport of vapour from sublimating ice dominates the total hydration. Note this is not guaranteed, even in the $R_{\text{H}} \gg 1$ regime: adiabatic cooling during ascent freeze-dries large amounts of vapour into ice. Thus for there to be an excess hydration, sufficient mixing must occur for some or most of the ice to be sublimated back into vapour.

Figure 2(a)–(c) shows the evolution of the tracer totals $\mathcal{T}_v$, $\mathcal{T}_c$ and $\mathcal{T}_p$, their rate of change, and their retained fraction over time in simulation `control`. The tracer totals in figure 2(a) increase rapidly until a few seconds after plume forcing ends

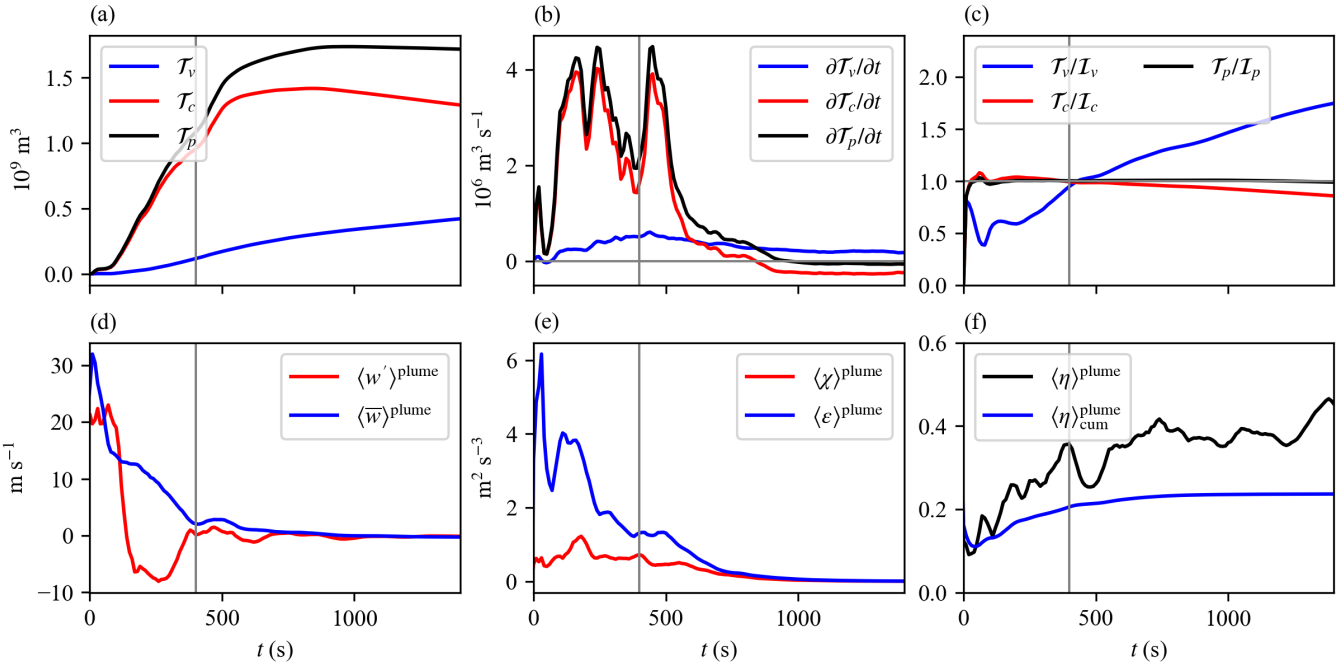

FIGURE 2 Evolution of tracers, vertical velocity, and mixing metrics in the stratified layer in simulation `control`. All quantities are averaged within the plume $\phi_p \geq 10^{-3}$ in the stratified layer $z \geq -L$. (a) Total vapour $\mathcal{T}_v$, ice $\mathcal{T}_c$ and passive tracer $\mathcal{T}_p$. (b) Rate of change of total vapour, ice and passive tracer. (c) Retained fraction of vapour, ice and passive tracer. (d) Turbulent vertical velocity $\langle w' \rangle^{\text{plume}}$ and mean vertical velocity $\langle w \rangle^{\text{plume}}$. (e) Buoyancy variance dissipation rate $\langle \chi \rangle^{\text{plume}}$ and TKE dissipation rate $\langle \varepsilon \rangle^{\text{plume}}$. (f) Instantaneous mixing efficiency $\langle \eta \rangle^{\text{plume}}$ and cumulative mixing efficiency $\langle \eta \rangle^{\text{plume}}_{\text{cum}}$ defined in (5). The grey vertical lines indicate the time $t = t_{\text{lim}}$ when plume forcing ends.

(indicated by a vertical grey line), when the majority of the plume fluid has entered the stratified layer. Note the slower increase in $\mathcal{T}_v$ compared to $\mathcal{T}_p$ and $\mathcal{T}_c$: relatively little vapour is directly transported into the stratified layer and some vapour is lost during ascent towards z_{max} due to adiabatic cooling. After plume forcing ends and the plume cap has collapsed, $\mathcal{T}_c$ begins to decrease. Sublimation of ice to form vapour begins much earlier, as shown by the increase in the retained vapour fraction $\mathcal{T}_v/\mathcal{I}_v$ in figure 2(c) from $t \approx 5$ s onwards, but $\mathcal{T}_c$ continues to increase because of direct transport of ice into the stratified layer and condensation of vapour due to adiabatic cooling during ascent. Once these processes cease around $t = 800$ s, $\partial_t \mathcal{T}_c$ becomes negative. There is a very gradual reduction in $\mathcal{T}_p$ at late times as the bottom of the plume falls slightly below $z = -L$. From $t \approx 800$ s onwards, there is an approximately constant conversion of ice into vapour as plume fluid descends whilst the plume cap relaxes owing to adiabatic warming as well as from continued mixing as the plume reaches equilibrium with the environment. Figure 2(c) shows that the retained fraction of vapour initially falls rapidly due to freeze-drying during ascent, then increases as mixing results in the sublimation of ice. From $t \approx 400$ s onwards, the retained fraction of vapour $\mathcal{T}_v/\mathcal{I}_v > 1$ so there is an excess hydration. Correspondingly, the retained fraction of ice $\mathcal{T}_c/\mathcal{I}_c < 1$.

3.3 | Evolution of mixing statistics

To quantify turbulent mixing and vertical transport by turbulent eddies in the plume, we consider plume averages of the mean and turbulent vertical velocity, and two mixing metrics: the turbulent kinetic energy (TKE) dissipation rate ε and the buoyancy variance dissipation rate χ, defined as

$$\varepsilon = \nu_{\text{tot}} \frac{\partial u_i}{\partial x_j} \frac{\partial u_i}{\partial x_j}, \quad \chi = \frac{\kappa_{\text{tot}}}{N_0^2} |\nabla b'|^2, \tag{4}$$

where ν_{tot} is the sum of the molecular and SGS viscosity, κ_{tot} is the sum of the molecular and SGS diffusivity of buoyancy and $b' = b - N_0^2 z \mathcal{H}(z)$ is the buoyancy perturbation from the background stratification. The variable ε acts as a sink of (turbulent) kinetic energy due to mixing; large values indicate energetic turbulent motions. The variable χ acts as a sink of potential energy

due to mixing by quantifying the irreversible conversion of available potential energy to background potential energy that results from the reduction of buoyancy gradients by mixing, thus quantifying the amount of dissipated energy that directly results in mixing of the buoyancy field (Davies Wykes et al., 2015; Howland et al., 2020). Together, χ and ε can be used to calculate the instantaneous mixing efficiency as $\eta = \chi/(\chi + \varepsilon)$, which quantifies the fraction of dissipated energy that results in mixing (e.g. Davies Wykes et al. (2015)). The cumulative mixing efficiency,

$$\eta_{\mathrm{cum}}(\boldsymbol{x}, t) = \frac{\int_0^t \chi \, \mathrm{d}t}{\int_0^t \chi \, \mathrm{d}t + \int_0^t \varepsilon \, \mathrm{d}t}, \tag{5}$$

is an integrated form of η which represents the energetic influence of a mixing event that occurs over a finite time period (Davies Wykes et al., 2015).

The vertical velocity is split into a turbulent and mean component by calculating an azimuthal average and a running mean over one buoyancy period $2\pi/N_0$. Here, the plume average $\langle\cdot\rangle^{\mathrm{plume}}$ is calculated from x-z cross-sections by averaging in the horizontal and vertical where $\phi_p \geq 10^{-3}$ and restricting to the stratified layer $z \geq -L$. The horizontal component of the average is weighted by the radius from the plume centreline to emulate a volume average. A test simulation with the full 3D volume average computed at runtime showed negligible difference with the 2D approximation. Later, when vertical shear is introduced in the stratified layer, the weighting is modified to use the radius from the centre of the intrusion. The decomposition of the vertical velocity is not calculated for the shear simulations since the plume is no longer approximately axisymmetric.

The vertical velocity and mixing statistics in simulation `control` are shown in figure 2(d)–(e). Shortly after penetration, the mean and turbulent vertical velocities are large in the plume as the central updraft dominates the average. Once the plume cap forms, with fluid subsiding and forming an intrusion, the mean vertical velocity decreases. Note that during formation of the plume cap up to $t \approx 400$ s, the turbulent vertical velocity is (on average) negative as plume fluid overturns and collapses. During this collapse, intense mixing between the plume and environment occurs. Evolution of $\langle\varepsilon\rangle^{\mathrm{plume}}$ is similar to the mean vertical velocity: initially large, then decreasing as subsiding fluid suppresses turbulent motions in the rising plume. Mixing is steady during collapse of the plume cap: $\langle\chi\rangle^{\mathrm{plume}}$ increases during penetration and then remains steady from $t \approx 200$ s to $t \approx 600$ s. Mixing gradually weakens as the plume reaches equilibrium with the environment at late times. The more gradual initial increase in $\langle\chi\rangle^{\mathrm{plume}}$ relative to $\langle\varepsilon\rangle^{\mathrm{plume}}$ occurs because the plume already has energetic turbulence at penetration but it takes some time for intense buoyancy gradients to become established between the plume and environment. Correspondingly, the mixing efficiency $\langle\eta\rangle^{\mathrm{plume}}$ in figure 2(c) increases over time. The cumulative mixing efficiency indicates that around 20% of the energy dissipated during convective penetration results in mixing.

4 | COMPETING EFFECTS OF SEDIMENTATION AND MIXING

In Part I, we explored the model regimes $R_{\mathrm{S}} \ll 1$, $R_{\mathrm{S}} \sim 1$, $R_{\mathrm{S}} \gg 1$, showing that when $R_{\mathrm{S}} \gtrsim 1$ then ice is not kept in suspension once fluid overturns near the maximum penetration height. Consequently, ice does not reach the edge of the plume cap where the most intense mixing between the plume and environment occurs, so formation of vapour via sublimation of ice is significantly limited. Previous studies have concluded that sedimentation strongly modulates vapour transport, but conclusions on the importance of this effect relative to small-scale mixing differ. Hassim and Lane (2010) found that mixing is more localised than the extensive regions of moistening in their simulations, leading to the conclusion that microphysical processes (such as sedimentation) prevail over the effects of small-scale mixing in determining vapour transport. Sang et al. (2018) found that turbulent mixing makes a significant contribution to the transport of small ice particles from the convective cloud top into the TTL environment. Smaller ice particles are less influenced by sedimentation, hence mixing has a more influential role in determining net hydration. These conclusions depend on the accuracy of the SGS turbulence parameterisation and the indirect measures used to assess mixing, via parameterised TKE in H10 and an inferred turbulent mixing coefficient in S18. In the following analyses we directly quantify mixing using the buoyancy variance dissipation rate. We consider simulations `control`, `weak_sed`, `sed`, and `strong_sed`, with $R_{\mathrm{S}} = 0, 0.06, 0.6, 7.2$, respectively. The dynamics and turbulent mixing are not influenced directly by sedimentation; we focus on the modulation of the hydration process by sedimentation and show that in the two extreme regimes $R_{\mathrm{S}} \gg 1$ and $R_{\mathrm{S}} \ll 1$, hydration of the stratified layer can be predicted using semi-quantitative models that predict vapour concentrations indirectly by using the temperature of fluid parcels which are determined by dynamics alone and encapsulate the effect of mixing. The differing conclusions in H10 and S18 can be viewed as corresponding to the two extreme

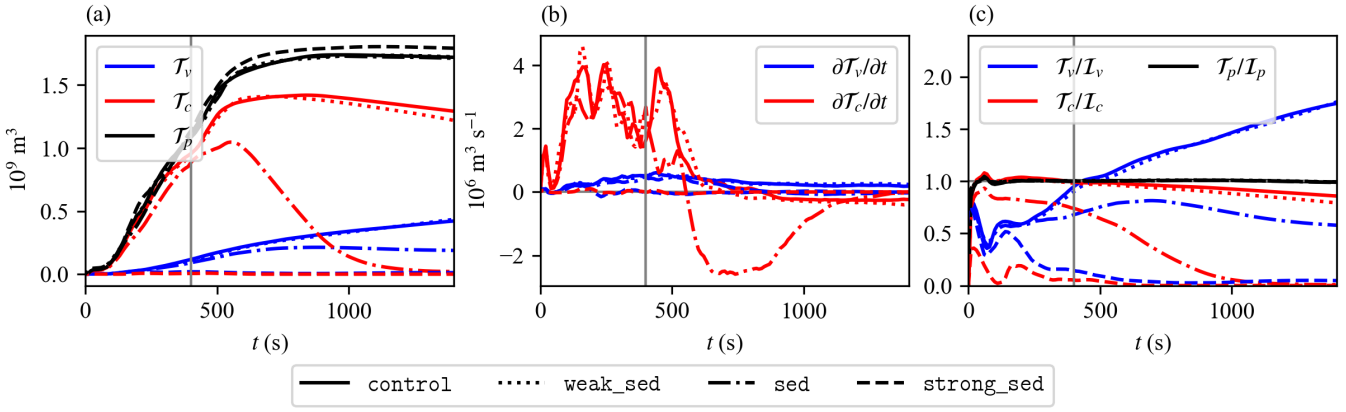

FIGURE 3 Comparison of tracer totals and vertical velocity in simulations `control`, `weak_sed`, `sed`, and `strong_sed`. (a) Total vapour $\mathcal{T}_v$, ice $\mathcal{T}_c$ and passive tracer $\mathcal{T}_p$. (b) Retained fraction of vapour, ice, and passive tracer. The vertical grey line indicates the time $t = t_{\text{lim}}$ when plume forcing ends.

regimes, $R_S \gg 1$ and $R_S \ll 1$, which are representative of cases in the real atmosphere where the mean size of ice crystals is relatively large or small, corresponding with a stronger or weaker mean sedimentation velocity.

4.1 | Evolution of moist tracers

As shown in Part I, in all of the simulations with varied R_S, some ice is lifted into the stratified layer by the strong central updraft in the plume. As the sedimentation velocity increases, ice falls out of suspension increasingly rapidly after reaching the plume cap. Correspondingly, vapour concentrations within the plume at late times are reduced. An additional observation compared to the shorter simulations with varied R_S shown in Part I is that even when w_s is relatively weak as in simulation `weak_sed`, ice sediments out of the plume at late times. Figure 3 quantifies the evolution of the moist tracer totals as in figure 2(a)–(c). In simulation `strong_sed`, the ice total $\mathcal{T}_c$ remains small at all times and the retained fraction rapidly decreases to zero. In simulations `weak_sed` and `control` the vapour and ice totals $\mathcal{T}_v$ and $\mathcal{T}_c$ grow monotonically whilst the plume is forced, after which $\mathcal{T}_c$ decreases as ice continues to sublimate to form vapour, increasing the retained fraction of vapour $\mathcal{T}_v/\mathcal{I}_v$. In the intermediate case where $R_S \sim 1$ in simulation `sed`, some ice is kept in suspension in the plume cap by strong turbulent eddies. Hence, during penetration, $\mathcal{T}_c$ and $\mathcal{T}_v$ increase roughly in line with simulation `control` and `weak_sed` and the retained vapour fraction increases due to sublimation of ice. Once plume forcing ends, the plume cap begins to collapse so any remaining ice begins to fall out of suspension, resulting in a sudden change in the sign of $\partial_t\mathcal{T}_c$. The total vapour $\mathcal{T}_v$ remains approximately constant as the flow relaxes, from $t \approx 800$ s onwards. Crucially, although the sedimentation velocity does not dominate the typical eddy velocity in simulation `sed`, the total hydration is approximately halved relative to simulations `control` and `weak_sed`.

4.2 | Semi-quantitative hydration models

In Part I, we found that the presence of ice at the edge of the plume cap, where the plume mixes with the most buoyant environmental fluid, is determined by the relative size of the typical turbulent eddy vertical velocity and the sedimentation velocity. Here, we extend this idea to show that the 'final' vapour distribution – following restratification of the environment once the plume settles and buoyancy contours are relaxed – can be predicted by 'semi-quantitative' models which use the temperature of fluid parcels only and are therefore determined by dynamics alone with no explicit modelling of mixing or moist processes. We use two semi-quantitative models based on 'fast' and 'slow' sedimentation regimes with $R_S \gg 1$ and $R_S \ll 1$, respectively, to predict the distribution of ϕ_v at the end of the simulation, $t = t_{\text{end}}$, and compare with the observed PDF in each simulation. The models are derived as follows:

- **Slow sedimentation (final T):** assume that eddies are strong enough relative to the sedimentation velocity to keep ice in suspension in the plume. Thus vapour condensed into ice remains in the plume so the vapour concentration is controlled by

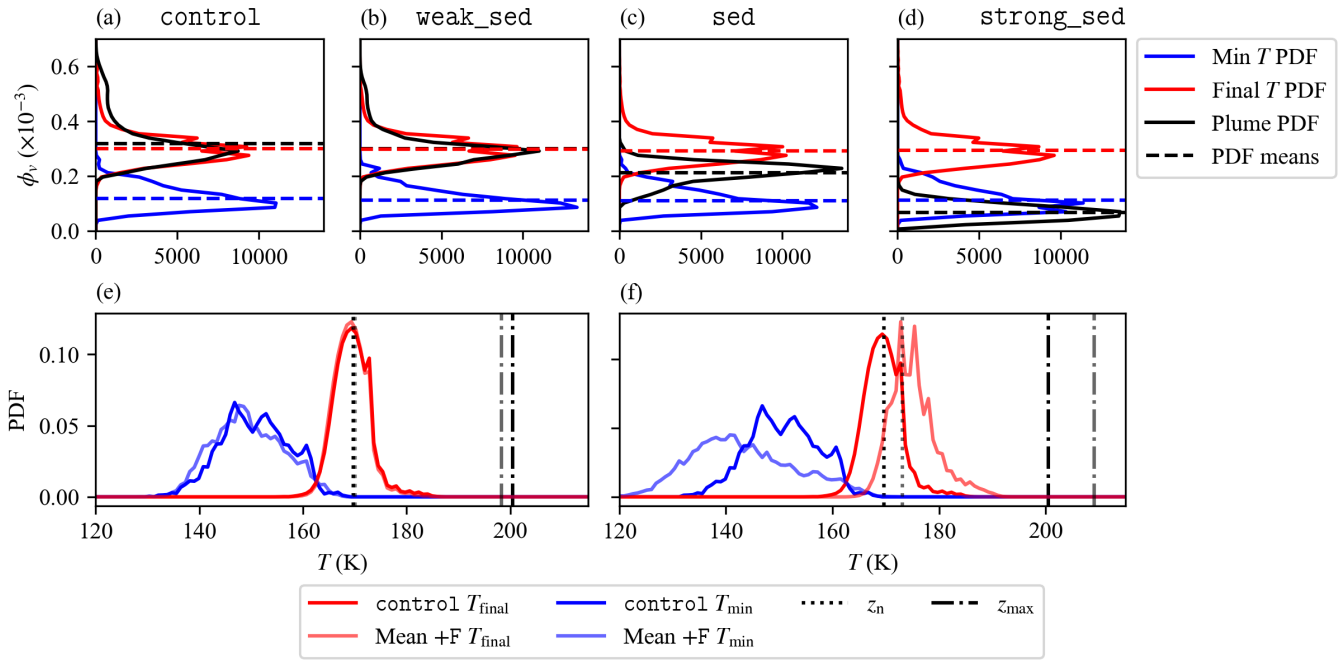

FIGURE 4 Comparison of semi-quantitative models of the vapour distribution and the observed distribution within the plume $\phi_p \geq 10^{-3}$ at time $t = t_{\text{end}}$ in simulations `control`, `weak_sed`, `sed` and `strong_sed`. (a)–(d) Comparison of observed PDF (black) with the Min T (blue) and Final T (red) predictions as described in the text. Horizontal dashed lines indicate the mean of each distribution. (e) Comparison of PDFs of the minimum temperature (blue) and final temperature (red) along parcel trajectories calculated as described in the text and averaged over the four simulations. (f) as (e) for an average of the three simulations with strong forcing (`+F`). Horizontal lines indicate the environmental temperature at $z = z_{\text{max}}$ (dot-dashed) and $z = z_{\text{n}}$ (dotted).

the saturation concentration once the plume reaches equilibrium with the environment at late times. Hence ϕ_v is controlled by the environmental temperature at the height z_f where each fluid parcel settles. To estimate the PDF of ϕ_v, compute a PDF of the heights of plume fluid with $\phi_p \geq 10^{-3}$ at $t = t_{\text{end}}$. Given a height z_f, the saturation vapour concentration is then $\phi_{vs}(T_{\text{final}})$ where

$$T_{\text{final}} = T_0 + \Theta N_0^2 z_f - \Gamma(z_f + H). \tag{6}$$

and $\phi_{vs} = \phi_0 \exp(\alpha(\Theta b - \Gamma(z + H)))$ as defined in Part I. Henceforth we refer to this as the 'Final T' model.

- **Fast sedimentation (minimum T):** assume that the sedimentation velocity dominates the eddy velocity, so that ice sediments out of the plume rapidly. Thus any vapour condensed into ice is lost from the plume so the vapour concentration is determined by the saturation concentration at the minimum temperature along each fluid parcel trajectory. To estimate the PDF of ϕ_v, we compute a set of parcel trajectories from x-z cross-sections through the plume centreline of the vertical and horizontal velocity at intervals of $\Delta t = 10$ s. We initiate 64 trajectories at random points within the plume $\phi_p \geq 10^{-3}$ and within the height range $-9.8\,\text{km} \leq z \leq -1.4\,\text{km}$ every 10 s from $t = 0$ to $t = 400$ s. Trajectories are propagated to the end of the simulation at time $t = t_{\text{end}}$ and rejected if the trajectory ends outside the plume. We compute a PDF of the minimum temperature T_{min} along the ~ 1200 valid trajectories. To account for the use of 2D data, the contribution of each trajectory to the PDF is weighted by its radial distance from the plume centreline. The PDF of ϕ_v is then computed using $\phi_{vs}(T_{\text{min}})$. Henceforth we refer to this as the 'Min T' model.

Figure 4(a)–(d) compares the Final T and Min T models with the observed vapour distribution at $t = t_{\text{end}}$ in the four simulations with varied sedimentation velocity. The horizontal dashed lines indicate the mean of the model and observed distributions to aid comparison. Figure 4(e) shows the PDFs of T_{min} and T_{final} in the Min T and Final T model, respectively, and the environmental temperature at the equilibrium height $z = z_{\text{n}}$ and the maximum penetration height $z = z_{\text{max}}$, averaged over the four simulations since the temperature distributions are qualitatively similar between simulations as the dynamics are unaffected by the variation

in w_s. Figure 4(e) also shows the environmental temperature at the neutral buoyancy height $z = z_n$, where fluid parcels eventually settle on average, and at $z = z_{max}$, representing the largest environmental temperature accessible via mixing.

As expected from our findings in Part I, the observed vapour concentration PDF at $t = t_{end}$ in simulations `control` and `weak_sed`, with $R_S = 0$ and $R_S \ll 1$ respectively, closely matches the Final T PDF. There is a small discrepancy between the Final T model and the observed distribution at large ϕ_v because the flow has not fully relaxed by the end of the simulation, so the warmest fluid parcels (carrying the largest vapour concentrations) have not yet relaxed to the environmental temperature. In simulation `strong_sed`, with $R_S \gg 1$, the observed vapour distribution more closely matches the Min T model, though on average ϕ_v is overestimated by the model because of continued mixing between the plume and environment as the intrusion spreads. This mixing reduces ϕ_v below $\phi_{vs}(T_{min})$ because of dilution with completely dry environmental fluid and the absence of ice. Note that the reduction in vapour concentrations does not reduce the total hydration – which is not fully captured by the observed PDF – since the total vapour is simply shared among a larger volume.

These results show that semi-quantitative models based on dynamics alone are able to produce reasonable estimates of the vapour PDF following relaxation of the flow, given knowledge of the sedimentation regime determined by R_S. The models as described are limited to predicting the distribution of vapour only. However, given additional knowledge of the partitioning of moisture between ice and vapour, determined by R_H, and the plume tracer flux at penetration, then a prediction for the total hydration can be formulated.

5 | ROLE OF CONVECTIVE INTENSITY IN CONTROLLING HYDRATION

We now consider simulations `control+F`, `sed+F` and `strong_sed+F` in which the plume forcing strength, quantified by the integral source buoyancy flux F_0, is four times larger than in simulation `control`, thus increasing the 'convective intensity'. In convective penetration of a buoyant plume into a stratified layer, the maximum penetration height, z_{max}, is directly linked to the convective intensity via the scaling relation $z_{max} \sim F_0^{1/4}$ (Briggs, 1965; Devenish et al., 2010; Powell et al., 2024), assuming that the environmental stratification N_0 is fixed. D18 proposed that z_{max} is a key parameter to characterise the hydration impact of a convective overshoot, since this determines the maximum environmental temperature accessible to the plume via mixing. Penetration to a greater maximum height permits mixing with relatively warmer stratospheric air, thereby increasing ϕ_{vs} further and allowing sublimation of a larger amount of ice. This effect relies on the presence of ice in the plume and is therefore sensitive to the effects of sedimentation which competes with stronger eddy velocities in the plume when the forcing is stronger. Here, we verify the role of convective intensity in controlling hydration, then explore the modulation of its influence by sedimentation and the influence of convective intensity on turbulent mixing.

5.1 | Influence on hydration

Figure 5 shows cross-sections of the flow evolution and figure 6 shows the evolution of the moist and passive tracers and mixing metrics over time as introduced in § 3. Comparing the vapour total $\mathcal{T}_v$ in simulations `control` and `control+F` in figure 6(a) shows that the total hydration is approximately doubled, supporting the conclusion of D18. According to integral plume theory (Morton et al., 1956), the effect of quadrupling F_0 in the strong forcing simulations is to increase the maximum penetration height $z_{max} \sim F_0^{1/4}$ by a factor of $\sqrt{2}$ and to increase the azimuthally averaged vertical velocity on the plume centreline $\overline{w} \sim F_0^{1/3}$ by a factor of $4^{1/3} \approx 1.6$. Thus the plume rises more quickly towards its maximum height and the upward flux of tracers into the stratified layer is increased. Note that the source tracer flux $F_0^{(\phi)}$ is unchanged between the control and strong forcing simulations, so the *total* transport of (passive) tracer into the stratified layer is the same, but tracer reaches the stratified layer more quickly when the forcing is stronger. The increased vertical velocity on the plume centreline results in a larger direct transport of tracers into the stratified layer. This is reflected in the more rapid increase in $\mathcal{T}_p$ in figure 6(a). Increasing the convective intensity also increases the mean buoyancy in the plume (which scales with F_0 in the same way as the mean vertical velocity), supporting larger saturation vapour concentrations, further increasing direct transport. The increased maximum height is clear in figure 5, allowing the plume to perturb the $b = 3.5\,\mathrm{m\,s^{-2}}$ contour in the strong forcing simulations compared to the $b = 2.0\,\mathrm{m\,s^{-2}}$ contour in simulation `control`. Hence the plume accesses more buoyant (i.e. warmer) environmental fluid higher in the stratified layer, allowing more ice to sublimate to form vapour, as shown by the more rapid increase in the retained vapour fraction $\mathcal{T}_v/\mathcal{I}_v$ in simulation `control+F` compared to `control` in figure 6(b). Although the total hydration is larger in `control+F` relative to `control`, note from figure 6(c) that there is no longer an excess hydration. During ascent towards z_{max}, a larger amount of

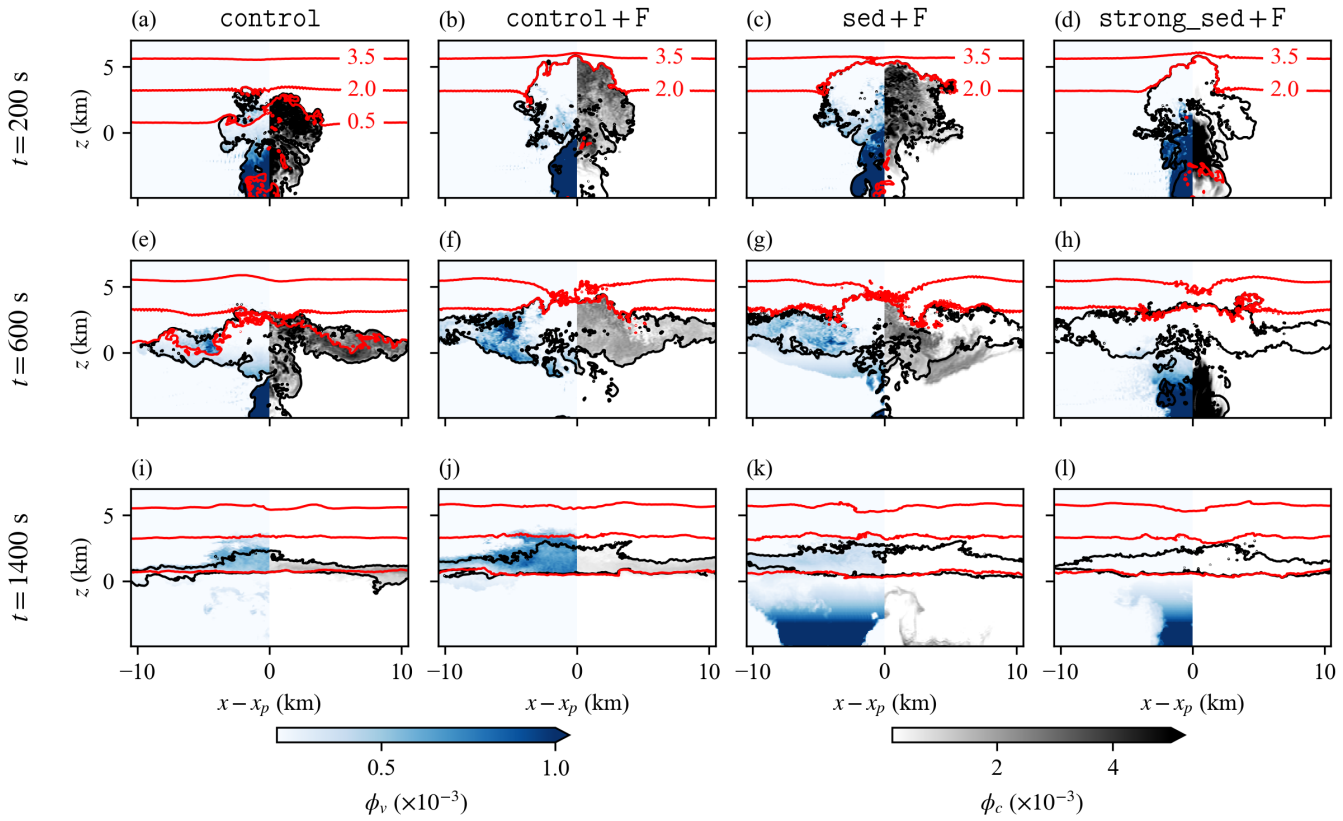

FIGURE 5 Snapshots of simulations `control`, `control+F`, `sed+F` and `strong_sed+F` at t = 200, 600, 1400 s. Each panel shows the vapour concentration ϕ_v (left) and ice concentration ϕ_c (right). The black outline indicates the plume contour $\phi_p = 10^{-3}$. In each panel, buoyancy contours are shown at 1.5 m s^{-2} intervals starting from b = 0.5 m s^{-2}. The b = 0.5 m s^{-2} contour has been omitted on the top two rows in the strong forcing simulations for clarity.

vapour is freeze-dried – note the lower minimum in the retained fraction of vapour in the strong forcing simulations. Therefore whilst access to more buoyant and warmer fluid in the environment is sufficient to increase the total hydration relative to the control forcing simulations, it is not sufficient to recover all of the vapour that is converted to ice during the penetration stage (bearing in mind also that more vapour is carried into the stratified layer during penetration, so $\mathcal{I}_v$ is larger).

The effect of increasing convective intensity on the flow is illustrated by the distributions of the minimum and final temperatures, T_{min} and T_{final}, for the strong forcing simulations shown earlier in figure 4(f) (calculated as described in § 4.2). Relative to simulation `control`, the distribution of final temperatures is shifted towards higher temperatures, reflecting both the more buoyant plume and its increased neutral buoyancy height, as well as mixing with more buoyant environmental fluid that raises the neutral buoyancy height further. The distribution of minimum temperatures is shifted towards lower temperatures, reflecting the greater maximum penetration height that results in further adiabatic cooling during ascent.

5.2 | Influence on turbulent mixing

The competition between sedimentation and mixing discussed in § 4 shifts in favour of mixing when the convective intensity increases because the stronger updraft velocity on the plume centreline more effectively counteracts the sedimentation velocity. Thus ice is carried deeper into the stratified layer and remains present in the plume cap for longer before sedimenting out. Note the more gradual decrease in $\mathcal{T}_c$ in figure 6(a) in simulations `sed+F` and `strong_sed+F` compared with simulations `sed` and `strong_sed` in figure 3(a). Figure 6(c) compares the plume averaged mean and turbulent vertical velocity between simulation `control` and averaged over the strong forcing simulations, showing that the increased convective intensity does not directly increase the strength of turbulent eddies – the mean turbulent vertical velocity in the plume is comparable. Thus the reduced

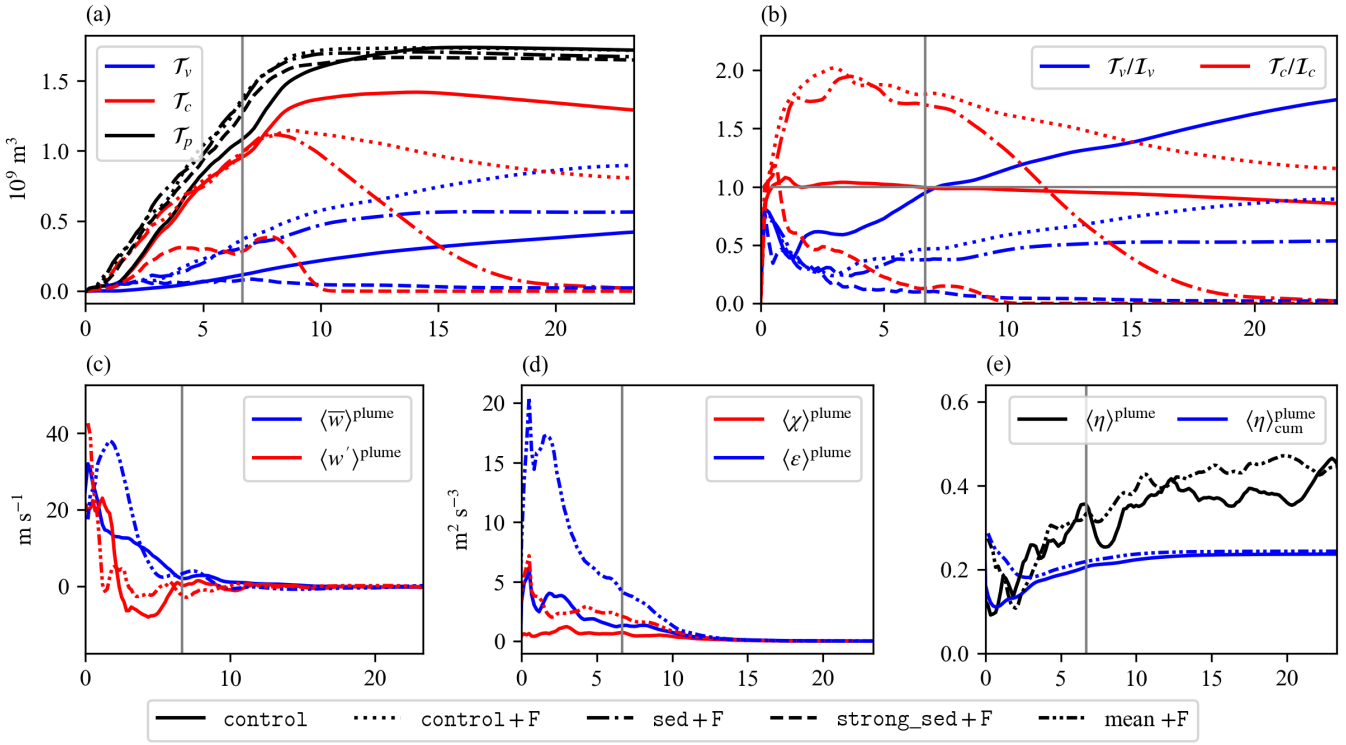

FIGURE 6 For simulations `control`, `control+F`, `sed+F`, and `strong_sed+F`: (a), (b) evolution of moist tracer totals as in figure 3(a) and (c), (c) – (e) mixing metrics as in figure 2.

influence of sedimentation in more intense convective plumes follows only from the increased and more persistent updraft velocity.

To assess the influence of convective intensity on turbulent mixing, in figure 6(d) and (e) we compare the mixing metrics in simulation `control` with the average of the strong forcing simulations. The results show that convective intensity does not result in more effective mixing between the plume and environment, in the sense that the mixing efficiency is unchanged. However, a stronger plume is more energetic so, in total, more energy is dissipated as the plume impinges on the stratified layer, resulting in stronger mixing between the plume and environment. This is demonstrated by the larger values of the plume average TKE dissipation rate $\langle\varepsilon\rangle^{\text{plume}}$, and increased mixing as shown by the larger values of the buoyancy variance dissipation rate $\langle\chi\rangle^{\text{plume}}$ throughout the simulation. Note that χ is a measure of the destruction of buoyancy gradients which depends on the magnitude of the buoyancy difference as well as the sharpness of the buoyancy gradients. We can estimate the buoyancy difference using characteristic scales from integral plume theory (Morton et al., 1956): the plume centreline buoyancy b_{max} at the maximum penetration height $z_{\text{max}} \sim F_0^{1/4}$ scales as $b_{\text{max}} \sim F_0^{2/3} z_{\text{max}}^{-5/3} \sim F_0^{1/4}$ and the environmental buoyancy b_{env} at z_{max} scales as $b_{\text{env}} \sim z_{\text{max}} \sim F_0^{1/4}$. Therefore the buoyancy difference between the plume and environment only weakly scales with F_0, whilst the increase in $\langle\chi\rangle^{\text{plume}}$ seen in figure 6(d) is roughly a factor of 3. Hence we conclude that the buoyancy gradients generated between the plume and environment, that are eroded by turbulent mixing, become sharper as the convective intensity is increased, meaning that the buoyancy difference occurs over a shorter distance. This suggests that the layer of intense buoyancy gradients formed at the edge of the plume cap during penetration is 'squeezed' when the plume is able to penetrate deeper into the stratified layer.

6 | THE INFLUENCE OF LARGE-SCALE VERTICAL SHEAR

In this final experiment we explore the influence of large-scale vertical shear on convective hydration of a stratified layer. In simulations `weak_shear`, `shear`, and `strong_shear`, the dynamics of the flow are significantly modified by the presence

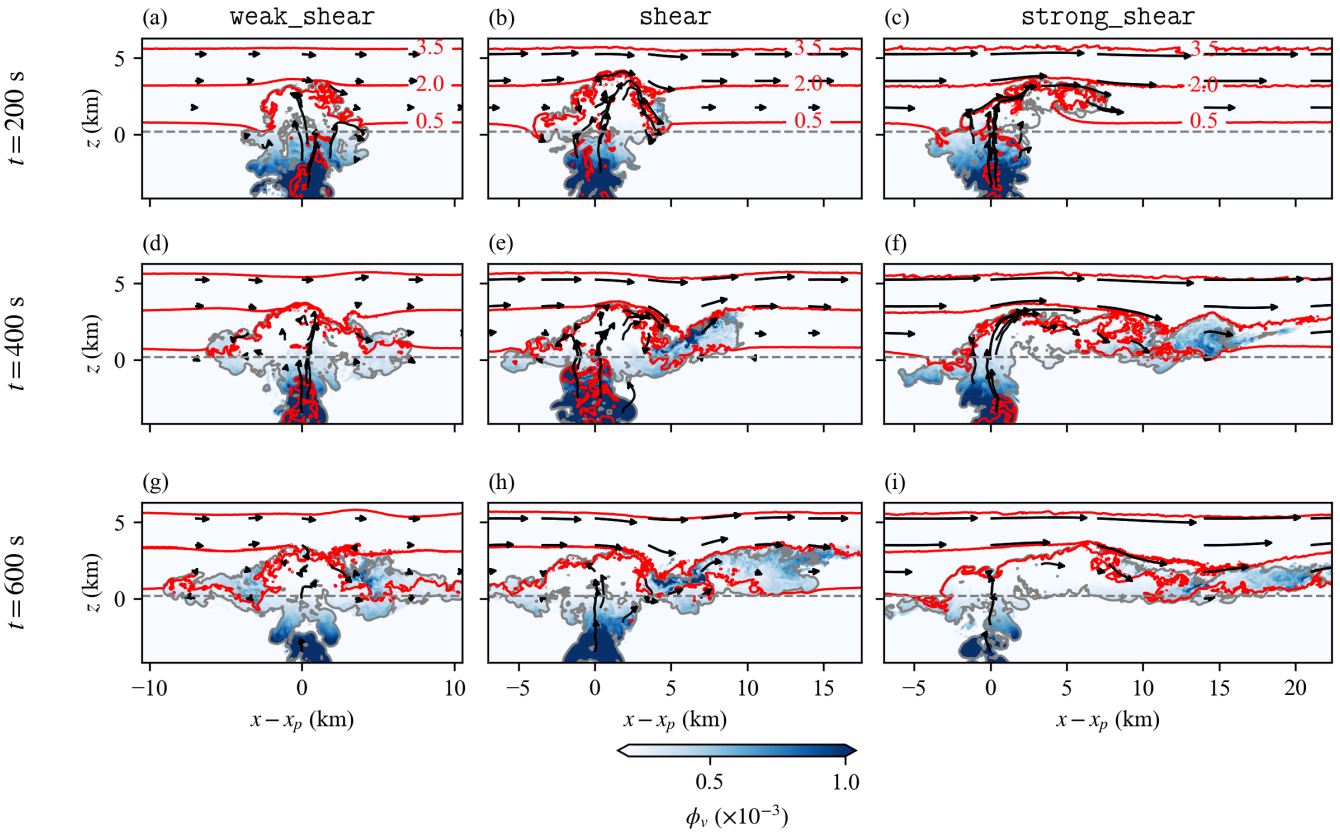

FIGURE 7 Flow summary as in figure 5, except only showing the vapour concentration ϕ_v, for simulations `weak_shear`, `shear` and `strong_shear`, with $R_{SH} \ll 1$, $R_{SH} \sim 1$, and $R_{SH} \gg 1$ respectively. The flow is indicated by black arrows with length proportional to the speed at the starting point. For these simulations, $R_H \approx 12$ and $R_S = 0$.

of a mean flow; we show that these structural changes are associated with distinct mechanisms that contribute to turbulent mixing between the plume and environment and act to increase hydration of the stratified layer.

Using the buoyancy-tracer volume distribution formalism introduced in Part I and by considering the spatial distribution of mixing as quantified by χ, we show how enhanced turbulent mixing results in an increased hydration of the stratified layer when large-scale shear is strong. Similarly, by exploring the internal wave and vortical response to convective penetration, we show that shear instabilities and internal gravity wave breaking contribute to the enhancement of turbulent mixing that increases the total hydration. Gravity wave breaking has previously been invoked as an important mechanism for turbulent mixing between convective overshoots and the surrounding TTL environment (e.g. Wang (2003); Lane and Sharman (2006); Wang et al. (2016); Homeyer et al. (2017) as well as H10 and D18). We identify a hydraulic jump-like feature that is consistent with earlier modelling studies (O'Neill et al., 2021) and a vortical response that is consistent with idealised numerical simulations (Lane, 2008) and comprehensive meteorological modelling studies (Dauhut et al., 2018). However, we emphasise that these mechanisms are influential to a varying extent depending on the large-scale shear rate but mixing between the plume and environment is primarily buoyancy-driven across all regimes.

Whilst our results are consistent with the aforementioned studies, others such as Sang et al. (2018) have found instead that vapour transport is reduced as environmental wind shear increases. Although Sang et al. (2018) note an increase in small-scale turbulent mixing, they found that a reduction in gravity wave breaking is the dominant influence of vertical shear near the tropopause. However, this conclusion appears to contradict the view that strong vertical wind shear tends to favour gravity wave breaking (e.g. Lane et al. (2003), and also noted in H10 and D18), which is supported by our simulations.

6.1 | Enhanced hydration and dynamical changes in the flow

Figure 7 illustrates the flow evolution using cross-sections of the vapour concentration in the three shear simulations. The velocity field is indicated by black arrows. Tracer totals are shown in figure 8(a) and the retained vapour fraction is shown in figure 8(b). The presence of vertical shear deforms the plume cap, resulting in the formation of an increasingly axisymmetric intrusion as the shear rate λ (and R_{SH}) increases. In simulation `strong_shear`, almost all mixed plume fluid (in the intrusion) lies downstream of the plume cap. There are three key consequences of this dynamical change. First, the maximum penetration height is shifted downstream, meaning fluid parcels take longer to rise to $z_{\max}$ – this is demonstrated by the delayed minimum in the retained vapour fraction in figure 8(b). Also, the lack of intrusion on the upstream side of the plume no longer shields rising plume fluid from the environment, meaning mixing between fluid parcels and the environment begins lower in the stratified layer for undiluted plume fluid on the upstream side of the rising plume. Finally, the downstream shift of $z_{\max}$ means that subsiding fluid which typically inhibits the upward flow of plume fluid into the stratified layer is dislocated from the rising plume, allowing more rapid transport of plume fluid into the stratified layer. This is clearly seen from the more rapid increase in $\mathcal{T}_p$ in figure 8(a).

Figure 8(a) shows that the total hydration $\mathcal{T}_v(t_{\mathrm{end}})$ and excess hydration fraction is increased in the strongest shear case in simulation `strong_shear` and slightly elevated in the intermediate case in simulation `shear`. The increased excess hydration fraction but similar evolution of $\mathcal{T}_p$ suggests that the increase in hydration arises from increased sublimation of ice rather than direct transport. Increased sublimation occurs owing to more intense mixing between the plume and environment that more effectively raises the temperature of mixed fluid parcels compared to the control simulation, as indicated by the increased deformation of the $b = 2.0\,\mathrm{m\,s^{-2}}$ contour in e.g. panel (e) and (f) of figure 7 compared with simulation `control`. The more effective mixing can also be seen by considering the distributions of the final vapour concentrations, final temperature and minimum temperature PDFs as described in § 4.2, which are shown in figure 8(c)–(e). As the shear rate increases, T_{final} increases, consistent with figure 7 where it can be seen that the intrusion sits slightly higher in the simulations with stronger shear as the neutral buoyancy height is raised by mixing with warmer environmental fluid. The $T_{\min}$ distribution widens, supporting the earlier observation that some fluid parcels begin mixing with the environment earlier in their rise towards $z_{\max}$ when the intrusion is asymmetric, meaning these fluid parcels do not become as cool during ascent. The wider distribution of ϕ_v at $t = t_{\mathrm{end}}$ in `strong_shear`, and in particular the broader tail of the distribution at large concentrations, supports the conclusion that enhanced mixing forms warmer mixed fluid parcels, permitting larger vapour concentrations. The large differences in the shape of the ϕ_v PDF between the three shear simulations is representative of the fact that mixing is ongoing at the end of the shortened simulations.

Changes in the spatial distribution of the moist regions between the shear simulations in figure 7 are indicative of structural changes in the way that mixing occurs as the shear rate increases. Simulation `weak_shear` resembles earlier experiments without a mean flow, where regions with (relatively) large vapour concentrations form surrounding the base of the plume cap. When the shear rate is larger in simulations `shear` and `strong_shear`, the anomalously moist regions instead form downstream of the plume cap. Simulation `strong_shear` with $R_{\mathrm{SH}} \gg 1$ is similar to the $R_{\mathrm{SH}} \ll 1$ case in the sense that the moist anomalies are formed after fluid parcels subside from the maximum penetration height (i.e. at the far downstream end of the intrusion), though the moistened region is spread over a wider area as the intrusion is stretched downstream. In the $R_{\mathrm{SH}} \gg 1$ case, figure 7(f) appears to show a Kelvin-Helmholtz-like roll-up of the intrusion at $t = 400\,\mathrm{s}$, with two 'billows' resulting in significant perturbations of the buoyancy contours throughout the intrusion. The roll-up relaxes by $t = 15\,\mathrm{s}$, though intense mixing continues at the top of the intrusion, downstream of the maximum height at $x \approx 0.5\,\mathrm{m}$. Recall that the shear simulations are initially stable, so the formation of KH-like shear instabilities requires a local enhancement of the shear rate or reduction in the local stratification. Indeed, we show later that the large-scale shear flow induces a downward flow over the plume cap that locally enhances the shear rate, such that $\mathrm{Ri}_g \leq 1/4$, allowing shear instabilities to develop. The intermediate shear case with $R_{\mathrm{SH}} \sim 1$ in simulation `shear` is distinct from the strong shear case, with the formation of a hydraulic jump-like feature in figure 7(e) and (h), marked by constriction of the intrusion immediately downstream of the plume cap and expansion of the flow downstream of the constriction. Intense mixing occurs near the constriction, aided by warm environmental fluid pulled down from above the plume, forming a moist region that is relatively confined compared to the other shear simulations. Mixing continues downstream as the flow expands. Our results are consistent with O'Neill et al. (2021) where a hydraulic jump was identified in large-eddy simulations of overshooting convection when stratospheric winds are sufficiently strong. Our work suggests supercritical flow in the presence of strong vertical shear is indeed a mechanism for enhancing hydration of the stratosphere, though the hydraulic jump is not the main driver of mixing, which is primarily buoyancy-driven simply as the result of a turbulent plume impinging on more buoyant surroundings.

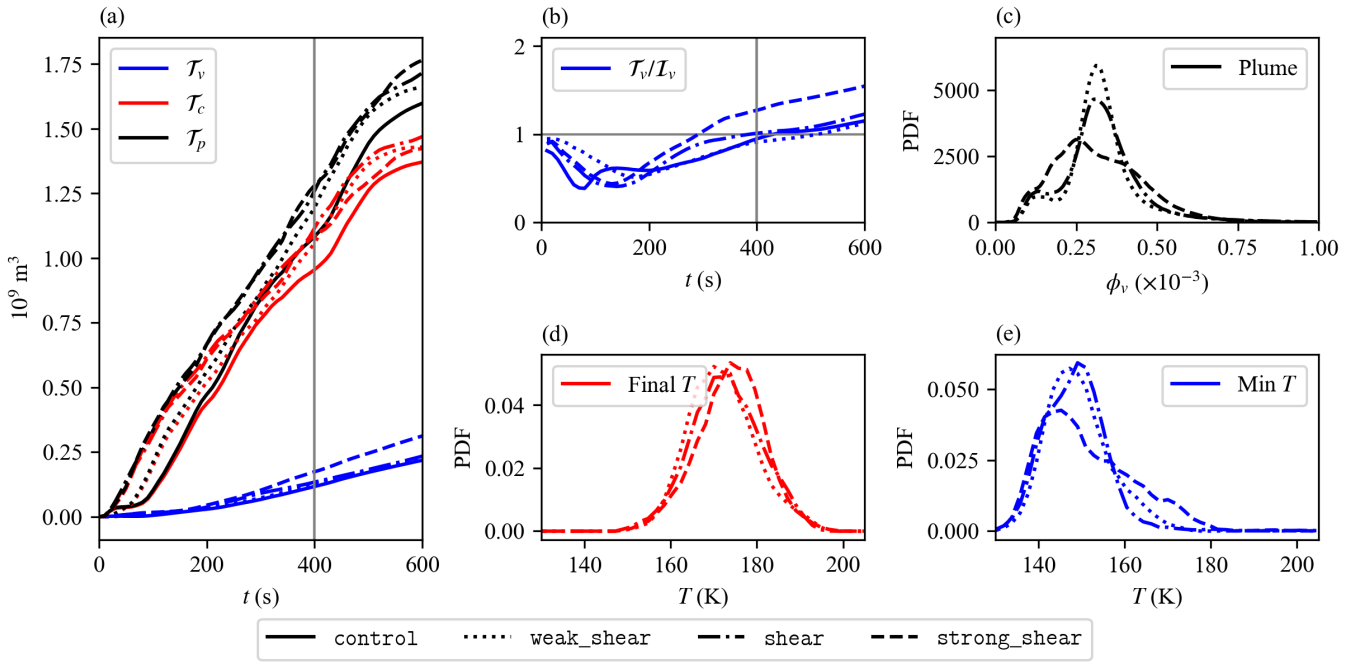

FIGURE 8 (a) Moist and passive tracer totals and (b) retained fraction of vapour and ice, as in figure 6, in simulations `weak_shear`, `shear`, and `strong_shear`. PDFs of the observed vapour concentration, final temperature and minimum temperature along parcel trajectories are compared in (c), (d) and (e) respectively.

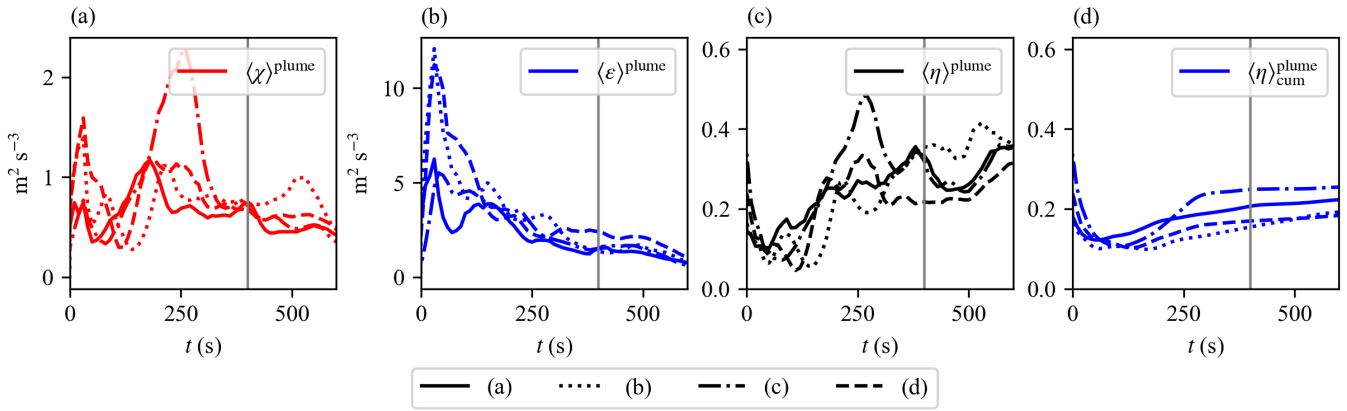

FIGURE 9 Time evolution of turbulent mixing metrics, introduced in § 3.3, in simulations `control`, `weak_shear`, `shear`, and `strong_shear`.

6.2 | Influence on mixing

Having established that strong large-scale vertical shear results increases hydration of the stratified layer via enhanced turbulent mixing, we quantify the influence of shear on mixing using the mixing metrics introduced in § 3.3, shown in figure 9, and the buoyancy-tracer volume distribution introduced in Part I. The buoyancy variance dissipation rate in figure 9(a) varies significantly over time, but is generally larger in the shear simulations compared to the control, especially in simulation `shear` with $R_{\text{SH}} \sim 1$. The large peak in $\langle\chi\rangle^{\text{plume}}$ at $t \approx 200$ s corresponds with initial formation of the hydraulic jump. The TKE dissipation rate in figure 9(b) is consistently larger in the shear simulations compared to the control, especially at early times in simulations `weak_shear` and `strong_shear`. In simulation `strong_shear` this is likely a result of the dislocation of the subsiding flow from the central updraft, which otherwise acts to limit the motion of turbulent eddies in the rising plume. The increase in ε in simulation `weak_shear` but not `shear` suggests that when $R_{\text{SH}} \lesssim 1$, the mean flow can enhance the motion of turbulent

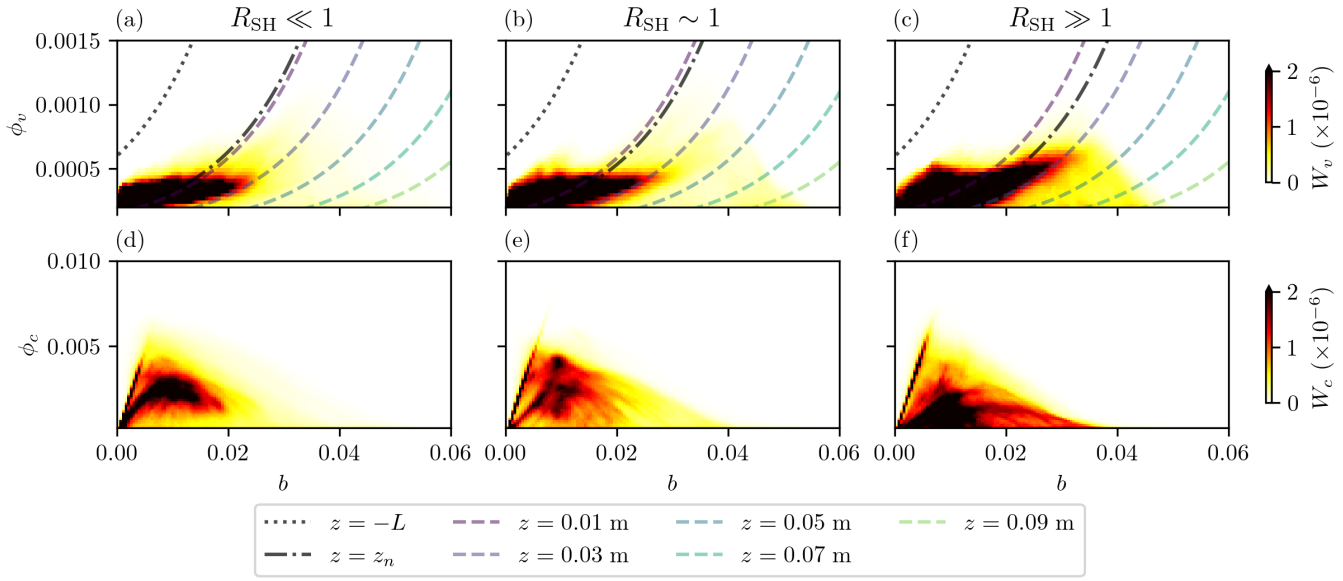

FIGURE 10 Buoyancy-vapour and buoyancy-ice volume distributions W_v and W_c at $t = t_{\text{end}}$ in simulations `weak_shear`, `shear` and `strong_shear`, with $R_{SH} \ll 1, \sim 1$ and $R_{SH} \gg 1$ respectively. In (a)–(c), saturation curves $\phi_v = \phi_0 \exp(\alpha(\Theta b - \Gamma(z + H)))$ are shown with $z = -L$ (black dotted), $z = z_n$ (black dot-dashed), and heights $z = 0.8, 2.4, 4.0$ km (dashed colour lines).

eddies but only when the shear is not so strong as to cause a downward flow onto the plume cap (discussed in detail later). The increase in χ without a corresponding increase in ε in simulation `shear` raises the instantaneous mixing efficiency in figure 9(c), reaching a plume average close to 50% at $t \approx 300$ s and resulting in a cumulative mixing efficiency in figure 9(d) that is $\sim 10\%$ larger than in simulation `control`.

Whilst the mixing efficiency is one contributor to the resulting hydration, the location of the strongest mixing is a more important factor given that mixing closer to the maximum height allows more effective warming of plume fluid and consequently greater hydration. The buoyancy variance dissipation rate χ is one way to examine the spatial distribution of mixing; large values indicate where intense buoyancy gradients are being broken down, i.e. where the strongest mixing occurs. As noted in Powell et al. (2024) and discussed in Part I, in the absence of a mean flow, a thin layer of large values of χ forms at the edge of the plume cap which is responsible for much of the mixing between the plume and the most buoyant environmental fluid accessible to the plume. In the presence of large-scale vertical shear, this layer of large χ is stretched downstream (see figure 7, increasing the area over which the most intense mixing between the plume and environment occurs. This is particularly evident in simulation `strong_shear`; in this case, layers of large χ form within the intrusion (not shown), which is indicative of shear instabilities associated with the KH-like roll-up of the intrusion at intermediate times. In simulation `shear`, the largest values of χ are found immediately downstream of the plume cap (not shown) at the hydraulic jump.

Although $\langle\chi\rangle^{\text{plume}}$ is not as large in simulation `strong_shear` compared to `shear`, the fact that the large values of χ are spread along the top edge of the plume cap and intrusion means the mixing is more effective in raising the buoyancy of mixed fluid parcels. This effect is well illustrated by the buoyancy-vapour and buoyancy-ice volume distributions W_v and W_c introduced in Part I and shown here at $t = 15$ s in the three shear simulations in figure 10. As the shear rate increases, the transport of ice-loaded fluid towards large b due to turbulent mixing is increased, meaning W_c is larger at large b. In turn, this allows a more significant proportion of ice to be sublimated to form vapour since ϕ_{vs} is larger, meaning W_v is also increased at large values of b. Importantly, the presence of large-scale shear does not influence the maximum buoyancy accessible via mixing; the increase in total hydration is a result of more *effective* mixing between the plume and environment in the sense that more fluid parcels are mixed with the most buoyant environmental fluid immediately above the plume, raising their temperature and permitting larger vapour concentrations.

6.3 | Influence on internal gravity wave response

Here we explore the effect of large-scale vertical shear on the internal wave response to convective penetration of a stably stratified layer and relate these changes to the enhanced turbulent mixing that increases total hydration. Numerical studies have suggested that a mean flow does not play a significant role in generating internal waves (Lane and Reeder, 2001), which is consistent with recent results suggesting that waves are generated within the turbulent plume (Powell et al., 2025b). Instead, the mean flow introduces an asymmetry in the wave response which we show is associated with formation of the hydraulic jump-like feature in simulation `shear` where $R_{\mathrm{SH}} \sim 1$. At larger shear rates, the mean flow introduces 'critical layers' where waves with a given frequency and wavenumber will break, leading to the development of turbulence and mixing in the region where they break (Lane et al., 2003; Lane and Sharman, 2006). Internal waves are also associated with a vortical response that induces an alternating downward and upward flow over the plume cap (Lane, 2008) that we show is responsible for decreasing the local gradient Richardson number Ri_g, supporting the formation of shear instabilities that locally enhance mixing.

Howland et al. (2021) explored shear-induced breaking of internal gravity waves in an idealised flow, showing that linear ray-tracing theory is qualitatively useful in describing refraction of waves by the shear despite the development of strong non-linearities which invalidates the assumption of a slowly-varying background. Motivated by this conclusion, we use ray tracing to explore the effect of a mean flow with linear shear $\boldsymbol{U} = \lambda z \hat{\boldsymbol{x}}$ in the presence of a linear stratification $b = N_0^2 z$. The dispersion relation for internal gravity waves in a linear stratification is

$$\omega^2 = N_0^2 \frac{k_h^2}{k_h^2 + k_z^2}, \tag{7}$$

where k_h and k_z are the horizontal and vertical wavenumber, respectively. In the presence of a mean flow, the *extrinsic* frequency Ω observed travelling with the mean flow $\boldsymbol{U}$ satisfies the (stationary) dispersion relation in (7). This is distinct from the *intrinsic* frequency,

$$\omega = \boldsymbol{U} \cdot \boldsymbol{k} + \Omega = \lambda z k_h + N_0 \frac{k_h}{\sqrt{k_h^2 + k_z^2}}, \tag{8}$$

measured by a stationary observer, where $\boldsymbol{k} = (k_h, k_z)$ is the wavevector and we have assumed that the large-scale shear may be treated as slowly-varying relative to the wave period (Sutherland, 2010). With respect to a stationary observer, an internal wave will propagate along a ray whose position $\boldsymbol{x}$ is determined by the ray tracing equations,

$$\frac{\mathrm{d}\boldsymbol{x}}{\mathrm{d}t} = \nabla_{\boldsymbol{k}}\, \omega, \quad \frac{\mathrm{d}\boldsymbol{k}}{\mathrm{d}t} = -\nabla \omega, \tag{9}$$

where $\nabla_{\boldsymbol{k}}$ is the gradient in wavenumber space. Waves encounter a 'critical level' when the vertical wavenumber k_z becomes infinite and the extrinsic frequency drops to zero, meaning upward propagating rays appear to bend over and become horizontal. As an internal wave beam approaches its critical level, the wave amplitude and (in the mean flow we consider) the vertical wavenumber grows until instabilities develop which cause the wave to break and drive turbulence. In the case of a linear shear, the intrinsic frequency ω and horizontal wavenumber k_h are conserved along a ray. Thus an internal wave beam encounters its critical level at a height z_c, determined by setting $\Omega = 0$ in (8), where

$$z_c = \frac{\omega}{\lambda k_h}. \tag{10}$$

We therefore expect that as the shear rate λ increases, waves with a given frequency and (horizontal) wavenumber encounter their critical level at a lower height. In particular, low frequency waves with large horizontal wavenumbers (i.e. narrow wave beams) are more likely to break lower in the stratified layer, close to the height of the penetrating plume and downstream intrusion.

Figure 11(b)–(e) shows horizontal cross-sections of the vertical velocity in `control` and the three shear simulations at $t = 10\,\mathrm{s}$. Rays computed according to (9) and initialised at $x_0 = x_p, z_0 = 0$ are overlaid in green for $\omega/N_0 = 0.5, 0.9$ and $k_h = 1, 0.1\,\mathrm{km}^{-1}$. Although the ray calculation assumes a slowly varying background and entirely neglects the presence of the penetrating plume, it gives a qualitative sense of the behaviour of internal wave beams which propagate upwards and outwards from the plume cap. To give a sense of the time-dependence of the wave response, figure 11(a) shows a time series of the vertical velocity at a single height $z/z_{\max} = 1.1$ on the centreline of each simulation, shown by a red dot in panels (b)–(e).

An important observation from figure 11(a) is that the wave response in simulations `control` and `weak_shear` is one of propagating internal waves, with oscillations in the vertical velocity evident above the plume. However, no oscillation is seen in

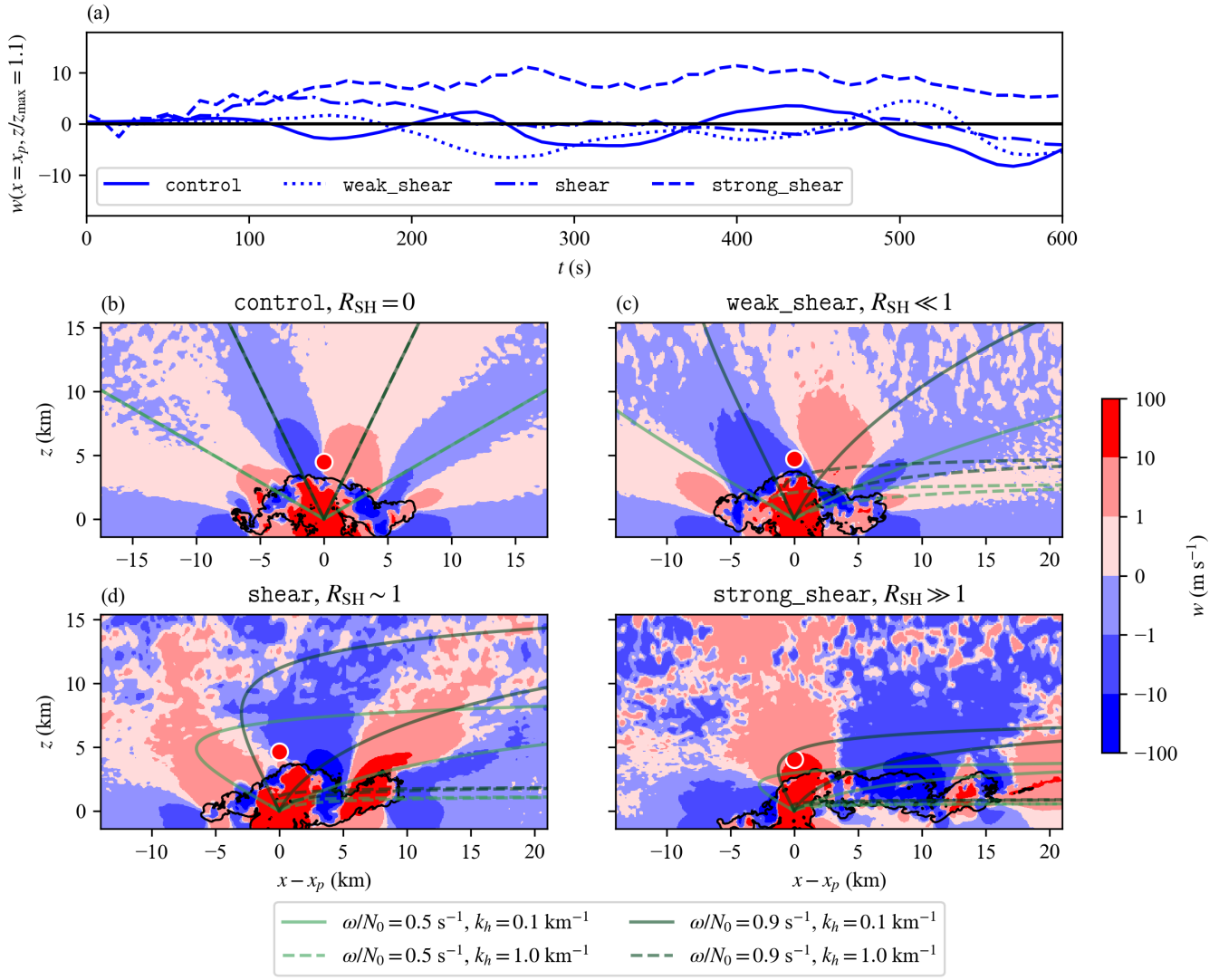

FIGURE 11 (a) Time series of vertical velocity w at $x = L_h/2$, $z/z_{max} = 1.1$ and (b)–(e) x-z cross-sections through the plume centreline of the vertical velocity at $t = 400$ s on a symmetric log scale in simulations `control`, `weak_shear`, `shear`, and `strong_shear`. Green lines are computed using ray tracing (as described in the text) initialised at $x = L_h/2$, $z = 0$ with fixed values of ω/N_0 and k_h shown in the legend. Red dots indicate the location of the time series of w shown in (a).

simulations `shear` and `strong_shear`, suggesting the large-scale shear is strong enough to prevent upstream propagation of internal waves. Instead, we observe features consistent with internal wave breaking; whilst the internal wave response in simulation `weak_shear` in figure 11(c) is similar to that seen in `control` except with slight asymmetries, the wave response when $R_{SH} \gtrsim 1$ in figure 11(d) and (e) is structurally different. Consistent with linear ray theory, the horizontal scale of the wave structures increases with shear rate because smaller scale waves break (note that the dashed rays with larger k_h become horizontal, i.e. break, lower in the domain). The structures also become incoherent at lower heights which is consistent with the theoretical prediction in (10) that internal waves encounter their critical levels at lower heights when the shear rate increases. We also note that the amplitude of the vertical velocity is larger immediately above the plume when the shear rate is larger, consistent with breaking of small-scale (high wavenumber) gravity waves. Similarly, the noisy signal observed well above the plume in simulations `shear` and `strong_shear` is consistent with the generation of turbulence and instabilities in the environment. The amplitude of the vertical velocity appears larger close to the plume, especially where large-amplitude perturbations of the intrusion are observed, e.g. near the hydraulic jump-like feature in `shear` and the KH-like structures in `strong_shear`.

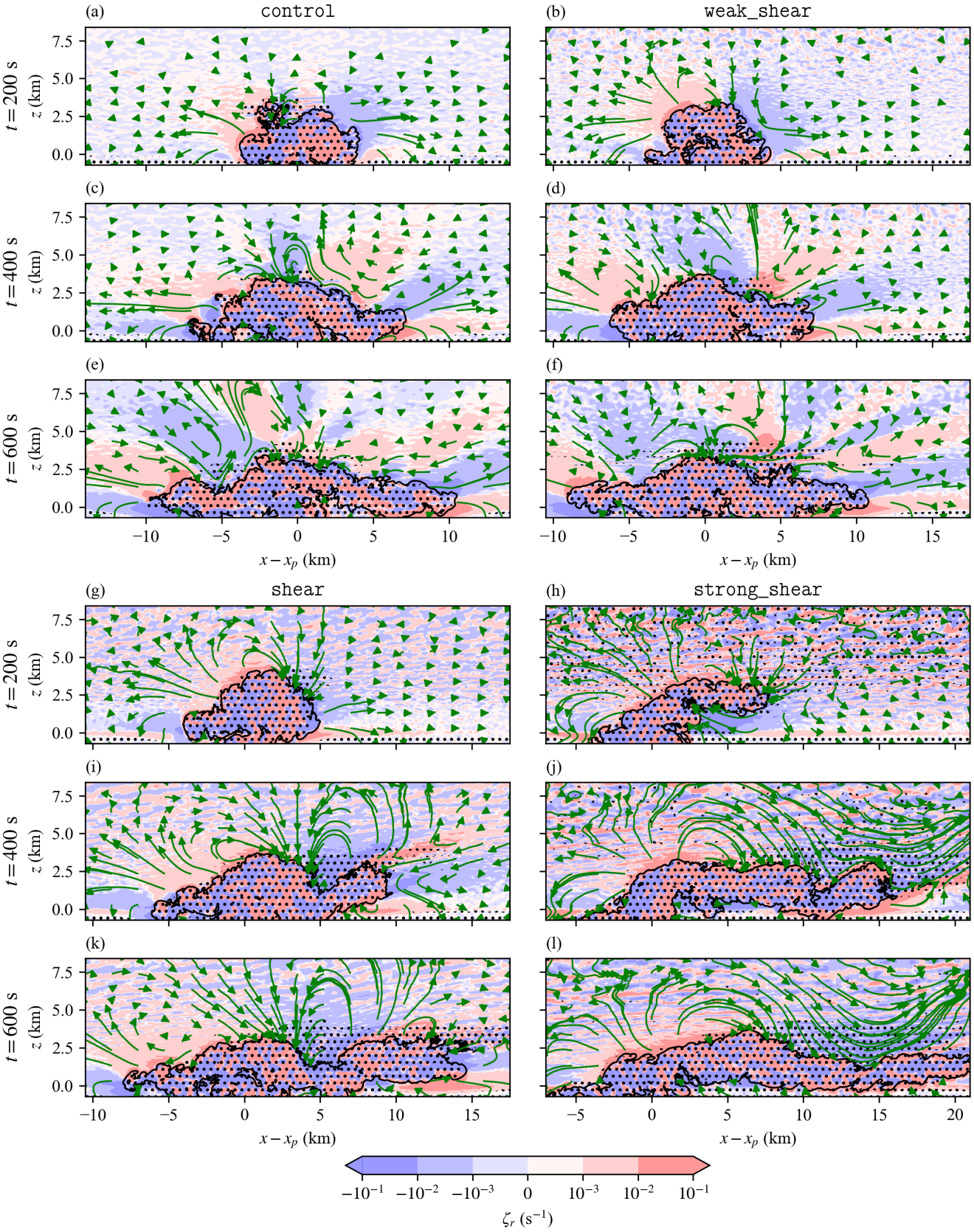

FIGURE 12 *x-z* cross-sections through the plume centreline of simulations `control`, `weak_shear`, `shear`, and `strong_shear` at t = 200, 400, 600 s showing the residual vorticity ζ_r (colour, symmetric log scale) and the residual circulation $\boldsymbol{u}_r$ (green arrows). Arrow length is proportional to the speed at the start point. The velocities are set to zero within the black line which indicates the plume contour $\phi_p = 10^{-3}$. Hatching indicates regions where the local Richardson number $\mathrm{Ri}_g \leq 1/4$, meaning the flow is susceptible to shear instability.

The internal wave response to penetrative convection is associated with a vortical response that is a half wavelength out of phase with the vertical velocity response, as shown in numerical simulations of a rising axisymmetric thermal by Lane (2008) where a 'secondary circulation' of vortices with alternating sign forms above the thermal. D18 identified these alternating vortices as a source of wind shear at the edge of a convective overshoot, suggesting this leads to instabilities and mixing. To explore this effect in the presence of large-scale vertical shear we define the residual circulation,

$$\boldsymbol{u}_r = \boldsymbol{u} - \lambda z \mathcal{H}(z), \tag{11}$$

and consider the out-of-plane residual vorticity ζ_r in an x-z cross-section of the flow, defined by

$$\zeta_r = \hat{\boldsymbol{y}} \cdot \nabla \times \boldsymbol{u}_r = \zeta_y - \lambda \mathcal{H}(z), \tag{12}$$

where $\zeta_y = \partial_z u - \partial_x w$ is the out-of-plane vorticity. Figure 12 shows three snapshots of the residual vorticity in simulations `control`, `weak_shear`, `shear`, and `strong_shear` at $t = 5, 10, 15$ s. The residual circulation is overlaid as green arrows with length proportional to the speed $|\boldsymbol{u}_r|$ at its starting point and velocities set to zero inside the plume. Arrows whose length is shorter than the size of the arrow head are not shown. Stippling indicates regions with $\mathrm{Ri}_g \leq 1/4$ that are susceptible to shear instability.

The circulation observed in figure 12 is consistent with the circulation described by Lane (2008) and D18; propagating internal waves form vortices of alternating sign above the plume cap. The residual circulation may enhance mixing by inducing shear instabilities via two pathways: either by increasing the local shear rate or by reducing the local buoyancy gradient. We note that regions with $\mathrm{Ri}_g \leq 1/4$ appear in the presence of both downward and upward flows, both of which can enhance the shear between the plume and environment (e.g. panel (e) and (f) of figure 12). Upward flows can also act to reduce the buoyancy gradient by separating buoyancy contours – note the right side of the plume cap in figure 12(d). The same behaviour is observed in simulation `weak_shear` despite slight asymmetries in the internal wave (and therefore vortical) response. The regions susceptible to shear instability are generally larger in `weak_shear` because of the weak environmental shear.

The vortical response in simulations `shear` and `strong_shear` is more complex: regions susceptible to shear instability extend further into the environment in both simulations. Simulation `shear` with $R_{\mathrm{SH}} \sim 1$ lies in a critical range where the gravity wave response is stationary. The formation of a hydraulic jump-like feature in simulation `shear` noted earlier appears to coincide with the formation of a stationary vortex downstream of the plume cap, where $\mathrm{Ri}_g \leq 1/4$, which recirculates the flow and produces a strong downward flow on the plume cap that acts to enhance mixing. Re-adjustment of the perturbed flow downstream of the jump acts to lift up the far end of the intrusion. The time when the recirculating vortex is strongest coincides with the peak in $\langle \chi \rangle^{\mathrm{plume}}$ in figure 9. The regimes in which a hydraulic jump forms can be deduced by defining a Froude number Fr in terms of the mean-flow velocity U at the obstacle height h,

$$\mathrm{Fr} = \frac{U}{N_0 h} = \frac{\lambda z_{\max}}{N_0 z_{\max}} = \frac{\lambda}{N_0}, \tag{13}$$

where h is chosen to be the maximum penetration height $z_{\max}$ (Homeyer et al., 2017; O'Neill et al., 2021). A hydraulic jump is expected to form when the flow is 'supercritical' with $\mathrm{Fr} > 1$, though 2D modelling and observations have shown that they may form when $\mathrm{Fr} \gtrsim 0.4$ (Durran, 1986). In simulation `shear`, $\mathrm{Fr} = 0.5$. The vortical structure and residual circulation in simulation `strong_shear` is distinct from simulation `shear`: instead of a stationary response, a downward flow forms over the downstream end of the intrusion. The downward flow results in a horizontally extended region where shear instabilities may form owing to the increased local shear rate. The observation of KH-like structures in the intrusion at $t = 400$ s coincides with the broad region where $\mathrm{Ri}_g \leq \frac{1}{4}$. However, the enhanced buoyancy gradient from the downward flow appears to limit the amplitude of the KH structure from $t \approx 400$ s onwards, a process which has been noted in idealised simulations of stratified shear flows (VanDine et al., 2021).

7 | DISCUSSION AND CONCLUSIONS

In this paper we use large-eddy simulations of an idealised model of convective hydration of the TTL to explore the role of ice sedimentation, convective intensity, and large-scale vertical shear. We represent convective overshooting as a turbulent buoyant plume penetrating into a linearly stably stratified layer carrying two temperature-dependent tracers that represent vapour and

ice which sediments downward at a fixed velocity. A scaled-down version of the geophysical problem is simulated so that the turbulent spectrum is better resolved compared to previous studies in the literature whilst maintaining a low computational cost. Simulation parameters were chosen to be representative of the TTL. This study is analogous to numerical studies of convective overshoots in the literature (Hassim and Lane, 2010; Sang et al., 2018; Dauhut et al., 2018), with the added advantage of using a model that allows exploration of a wide range of regimes, direct control of microphysical processes such as the strength of sedimentation, and reduced sensitivity to the representation of SGS turbulence. The use of a minimal moisture model that retains only simple representations of the essential microphysical processes also aids interpretation of the results.

The competition between sedimentation, which acts to remove ice from the plume, and mixing, which acts to convert ice to vapour, was addressed by varying the sedimentation velocity. We showed that semi-quantitative models of hydration based on dynamics alone provide estimates of the distribution of vapour concentrations at late times, after the flow relaxes. When the sedimentation velocity is weak relative to turbulent eddy velocities in the plume, the observed vapour concentrations are controlled by the environmental temperature at the equilibrium height $z = z_{\mathrm{n}}$ where plume fluid settles at late times because ice is kept in suspension so the plume is always at saturation. Mixing with buoyant fluid surrounding the plume acts to raise the equilibrium height above the height that would be predicted based on the buoyancy in the plume at penetration. Thus measuring z_{n} encapsulates the effect of mixing in raising the temperature of mixed fluid parcels in the plume. Conversely, when the sedimentation velocity is close to or stronger than the typical turbulent vertical velocity in the plume then ice settles out before plume fluid is warmed by mixing with the environment, decreasing the total hydration of the stratified layer. In this case, observed vapour concentrations can be predicted by measuring the maximum height that parcel trajectories reach, where the minimum temperature is attained. Although mixing as the intrusion spreads further dilutes vapour concentrations, the total hydration is unaffected.

Simulations with varied sedimentation velocity were repeated with the plume forcing quadrupled in strength, thus increasing the 'convective intensity' of the plume, to test the Dauhut et al. (2018) hypothesis that stronger plumes increase the total hydration by penetrating deeper and mixing with more buoyant environmental fluid. Our results confirm this hypothesis; for all values of w_s, the total hydration is increased. The influence of sedimentation is reduced as convective intensity increases (figure **??**) since the central updraft becomes stronger and mixing becomes more intense, so ice is kept in suspension for longer and more rapidly mixed with the environment. Although the plume can access more buoyant environmental fluid when the convective intensity is greater, the energetic efficiency of the mixing remains the same (figure 6). This conclusion is perhaps expected since increasing F_0 does not introduce any mechanisms that could result in more energetically efficient mixing. However, a stronger plume is warmer and more energetic, resulting in more energetic turbulence and mixing as well as increasing the direct transport of vapour into the stratified layer.

Finally, we showed that large-scale vertical shear has a strong influence on turbulent mixing and hydration of the stratified layer, with significant differences in the spatial distribution and intensity of mixing depending on the shear rate. Hydration of the stratified layer is increased when the shear rate is strong as a result of enhanced mixing between the plume and environment (figure 8). This supports the conclusion of Homeyer et al. (2017) that hydration is enhanced when there are strong storm-relative winds, which promote gravity wave breaking, but contrasts with the conclusion of Sang et al. (2018). As the shear rate increases, a larger proportion of the internal gravity wave spectrum generated by the plume is susceptible to breaking at heights close to the plume (figure 11). In the absence of wave breaking when the shear is weak (or absent), the alternating succession of vortices above the plume enhances wind shear at the edge of the plume, resulting in shear instabilities that enhance mixing (figure 12), consistent with Dauhut et al. (2018). When the shear timescale is comparable to or stronger than the dynamical timescale of the plume, the vortical response is modified as internal waves can no longer propagate upstream. The region of intense mixing between the plume and environment that is typically found at the edge of the plume cap extends into the intrusion (figure 12). In a critical range of shear rates, a vortex forms downstream of the plume cap that coincides with a hydraulic jump-like feature that locally enhances mixing. This is consistent with O'Neill et al. (2021) where hydraulic jumps were identified as a mechanism for hydration of the extratropical stratosphere – note that our study is relevant to both the tropics and extratropics, since the dynamical setup is similar, though hydration in the tropics is more influential globally due to transport by the Brewer-Dobson circulation. When the shear rate is sufficiently large, the downstream intrusion becomes widely susceptible to shear instabilities that enhance turbulent mixing over a broad spatial region, resulting in more effective mixing between plume fluid and the most buoyant environmental fluid immediately above the plume that increases the total hydration.

Whilst our results are consistent with the analogous numerical modelling studies by Hassim and Lane (2010), Sang et al. (2018) and Dauhut et al. (2018) in many respects, there are important differences, particularly with respect to the role of vertical shear and gravity wave breaking. We found that large-scale shear increases net hydration by enhancing mixing, which directly

contrasts with Sang et al. (2018) who concluded that the role of shear is largely to modulate gravity wave amplitudes rather than influence small-scale mixing. Our conclusions on the role of gravity wave breaking can also be contrasted with Sang et al. (2018) and Hassim and Lane (2010); whilst wave breaking appears to enhance mixing when the large-scale shear is strong, shear instabilities also contribute to turbulent mixing, and the hydration is only slightly elevated compared to simulations with weak or no vertical shear where gravity wave breaking is not observed. The primary driver of hydration in convective penetration of a stratified layer is buoyancy-driven mixing as the turbulent plume impinges on the more buoyant environment. Another contrasting viewpoint from our results is the complex interplay between dynamical and microphysical processes even in our idealised setup. The studies by Hassim and Lane (2010), Sang et al. (2018), and others in the literature (e.g. Homeyer et al. (2017); O'Neill et al. (2021)), seek to identify a dominant process that controls net hydration. However, we have shown that there are modulating factors that compete with one another in many different regimes, and it is not necessarily that case that all convective overshoots in the TTL sit in a narrow regime where a dominant process can be identified. For instance, as discussed in § 1, the range of shear rates found in the TTL is vast and, when translated into the language of our model, covers all of the R_{SH} regimes we consider. Across these regimes, mixing is primarily buoyancy-driven, but enhanced by distinct mechanisms depending on the strength of the large-scale shear.

ACKNOWLEDGMENTS
CWP acknowledges funding from EPSRC grant EP/T517846/1.

CONFLICT OF INTEREST
The authors declare no potential conflict of interests.

DATA AVAILABILITY STATEMENT
Simulation data and scripts used to generate figures are available upon request.

References

Briggs, G.A. (1965) A Plume Rise Model Compared with Observations. *J. Air Pollut. Control Assoc.*, 15(9), 433–438. doi:10.1080/00022470.1965.10468404.

Butchart, N. (2014) The Brewer-Dobson circulation. *Rev. Geophys.*, 52(2), 157–184. doi:10.1002/2013RG000448.

Dauhut, T., Chaboureau, J.P., Haynes, P. & Lane, T. (2018) The Mechanisms Leading to a Stratospheric Hydration by Overshooting Convection. *J. Atmospheric Sci.*, 75, 4383–4398. doi:10.1175/JAS-D-18-0176.1.

Davies Wykes, M.S., Hughes, G.O. & Dalziel, S.B. (2015) On the meaning of mixing efficiency for buoyancy-driven mixing in stratified turbulent flows. *J. Fluid Mech.*, 781, 261–275. doi:10.1017/jfm.2015.462.

Devenish, B.J., Rooney, G.G. & Thomson, D.J. (2010) Large-eddy simulation of a buoyant plume in uniform and stably stratified environments. *J. Fluid Mech.*, 652, 75–103. doi:10.1017/S0022112010000017.

Durran, D.R. (1986) Another Look at Downslope Windstorms. Part I: The Development of Analogs to Supercritical Flow in an Infinitely Deep, Continuously Stratified Fluid. *J. Atmospheric Sci.*, 43, 2527–2543.

Fueglistaler, S., Dessler, A.E., Dunkerton, T.J., Folkins, I., Fu, Q. & Mote, P.W. (2009) Tropical tropopause layer. *Rev. Geophys.*, 47(1), RG1004. doi:10.1029/2008RG000267.

Grabowski, W.W. (1998) Toward Cloud Resolving Modeling of Large-Scale Tropical Circulations: A Simple Cloud Microphysics Parameterization. *J. Atmos. Sci.*, 55(21), 3283–3298. doi:10.1175/1520-0469(1998)055<3283:TCRMOL>2.0.CO;2.

Hassim, M.E.E. & Lane, T.P. (2010) A model study on the influence of overshooting convection on TTL water vapour. *Atmos. Chem. Phys.*, 10(20), 9833–9849. doi:10.5194/acp-10-9833-2010.

Homeyer, C.R., McAuliffe, J.D. & Bedka, K.M. (2017) On the Development of Above-Anvil Cirrus Plumes in Extratropical Convection. *J. Atmospheric Sci.*, 74(5), 1617–1633. doi:10.1175/JAS-D-16-0269.1.

Howard, L.N. (1961) Note on a paper of John W. Miles. *J. Fluid Mech.*, 10(04), 509. doi:10.1017/S0022112061000317.

Howland, C.J., Taylor, J.R. & Caulfield, C. (2021) Shear-induced breaking of internal gravity waves. *J. Fluid Mech.*, 921, A24. doi:10.1017/jfm.2021.506.

Howland, C.J., Taylor, J.R. & Caulfield, C.P. (2018) Testing linear marginal stability in stratified shear layers. *J. Fluid Mech.*, 839, R4. doi:10.1017/jfm.2018.79.

Howland, C.J., Taylor, J.R. & Caulfield, C.P. (2020) Mixing in forced stratified turbulence and its dependence on large-scale forcing. *J. Fluid Mech.*, 898, A7. doi:10.1017/jfm.2020.383.

Lane, T.P. (2008) The vortical response to penetrative convection and the associated gravity-wave generation. *Atmos. Sci. Lett.*, 9(3), 103–110. doi:10.1002/asl.167.

Lane, T.P. & Reeder, M.J. (2001) Convectively Generated Gravity Waves and Their Effect on the Cloud Environment. *J. Atmos. Sci.*, 58(16), 2427–2440. doi:10.1175/1520-0469(2001)058<2427:CGGWAT>2.0.CO;2.

Lane, T.P. & Sharman, R.D. (2006) Gravity wave breaking, secondary wave generation, and mixing above deep convection in a three-dimensional cloud model. *Geophys. Res. Lett.*, 33(23), L23813. doi:10.1029/2006GL027988.

Lane, T.P., Sharman, R.D., Clark, T.L. & Hsu, H.M. (2003) An Investigation of Turbulence Generation Mechanisms above Deep Convection. *J. Atmos. Sci.*, 60(10), 1297–1321. doi:10.1175/1520-0469(2003)60<1297:AIOTGM>2.0.CO;2.

Liu, H.L. (2017) Large Wind Shears and Their Implications for Diffusion in Regions With Enhanced Static Stability: The Mesopause and the Tropopause. *JGR Atmospheres*, 122(18), 9579–9590. doi:10.1002/2017JD026748.

Miles, J.W. (1961) On the stability of heterogeneous shear flows. *J. Fluid Mech.*, 10(04), 496. doi:10.1017/S0022112061000305.

Morton, B.R., Taylor, G.I. & Turner, J.S. (1956) Turbulent gravitational convection from maintained and instantaneous sources. *Proc. R. Soc. Lond. A*, 234(1196), 1–23. doi:10.1098/rspa.1956.0011.

O'Neill, M.E., Orf, L., Heymsfield, G.M. & Halbert, K. (2021) Hydraulic jump dynamics above supercell thunderstorms. *Science*, 373(6560), 1248–1251. doi:10.1126/science.abh3857.

Powell, C.W., Haynes, P.H., Ming, A.D. & Taylor, J.R. (2025) Moisture transport by convective overshoots in the tropical tropopause layer. *Weather*,, wea.7689.doi:10.1002/wea.7689.

Powell, C.W., Haynes, P.H. & Taylor, J.R. (2024) Diagnosing tracer transport in convective penetration of a stably stratified layer. *J. Fluid Mech.*, 997, A48. doi:10.1017/jfm.2024.662.

Powell, C.W., Sutherland, B.R., Haynes, P.H. & Taylor, J.R. (2025) Internal waves generated by a plume impinging on a stratified fluid. *J. Fluid Mech.*, 1006, R2. doi:10.1017/jfm.2025.40.

Randel, W.J. & Jensen, E.J. (2013) Physical processes in the tropical tropopause layer and their roles in a changing climate. *Nat. Geosci.*, 6(3), 169–176. doi:10.1038/ngeo1733.

Sang, W., Huang, Q., Tian, W., Wright, J.S., Zhang, J., Tian, H. et al. (2018) A Large Eddy Model Study on the Effect of Overshooting Convection on Lower Stratospheric Water Vapor. *JGR Atmospheres*, 123(18), 10023–10036. doi:10.1029/2017JD028069.

Sunilkumar, S., Muhsin, M., Parameswaran, K., Venkat Ratnam, M., Ramkumar, G., Rajeev, K. et al. (2015) Characteristics of turbulence in the troposphere and lower stratosphere over the Indian Peninsula. *Journal of Atmospheric and Solar-Terrestrial Physics*, 133, 36–53. doi:10.1016/j.jastp.2015.07.015.

Sutherland, B.R. (2010) *Internal Gravity Waves*, 1st Edition. : Cambridge University Press.

VanDine, A., Pham, H.T. & Sarkar, S. (2021) Turbulent shear layers in a uniformly stratified background: DNS at high Reynolds number. *J. Fluid Mech.*, 916, A42. doi:10.1017/jfm.2021.212.

Wang, P.K. (2003) Moisture plumes above thunderstorm anvils and their contributions to cross-tropopause transport of water vapor in midlatitudes. *J. Geophys. Res. Atmospheres*, 108(D6), 1–15. doi:10.1029/2002jd002581.

Wang, P.K., Cheng, K.Y., Setvak, M. & Wang, C.K. (2016) The origin of the gullwing-shaped cirrus above an Argentinian thunderstorm as seen in CALIPSO images. *JGR Atmospheres*, 121(7), 3729–3738. doi:10.1002/2015JD024111.